Assimilative Mapping of Auroral Electron Energy Flux Using SSUSI Lyman-Birge-Hopfield (LBH) Emissions

J. Li[1], T. Matsuo[1] , and L. M. Kilcommons[1]

[1]Ann and H.J. Smead Department of Aerospace Engineering Sciences, University of Colorado Boulder, Boulder, CO, USA

Abstract Far ultraviolet (FUV) imaging of the aurora from space provides great insight into the dynamic coupling of the atmosphere, ionosphere, and magnetosphere on global scales. To gain a quantitative understanding of these coupling processes, the global distribution of auroral energy flux is required, but the inversion of FUV emission to derive precipitating auroral particles' energy flux is not straightforward. Furthermore, the spatial coverage of FUV imaging from Low Earth Orbit (LEO) altitudes is often insufficient to achieve global mapping of this important parameter. This study seeks to fill these gaps left by the current geospace observing system using a combination of data assimilation and machine learning techniques. Specifically, this paper presents a new data-driven modeling approach to create instantaneous, global assimilative mappings of auroral electron total energy flux from Lyman-Birge-Hopfield (LBH) emission data from the Defense Meteorological System Program (DMSP) Special Sensor Ultraviolet Spectrographic Imager (SSUSI). We take a two-step approach; the creation of assimilative maps of LBH emission using optimal interpolation, followed by the conversion to energy flux using a neural network model trained with conjunction observations of in-situ auroral particles and LBH emission from the DMSP Special Sensor J and SSUSI instruments. The paper demonstrates the feasibility of this approach with a model prototype built with DMSP data from 17 February 2014 to 23 February 2014. This study serves as a blueprint for a future comprehensive data-driven model of auroral energy flux that is complementary to traditional inversion techniques to take advantage of FUV imaging from LEO platforms for global assimilative mapping of auroral energy flux.

Plain Language Summary When energetic protons and electrons interact with the nitrogen gas molecules of the Earth's atmosphere at high latitudes, light emissions including ultraviolet emissions in the Lyman-Birge-Hopfield (LBH) band are created. Our goal is to make global maps of the energy flux of these particles using images of these LBH emissions observed by the Defense Meteorological System Program (DMSP) Low Earth Orbiting (LEO) satellites. This is a challenging task because ultraviolet imagers onboard LEO satellites can only provide partial coverage of the global high-latitude region and emissions are indirect measurements of the energy flux. To address these problems, we first determine a small set of global patterns from lots of DMSP data that efficiently explain how these LBH emissions vary over time. By using these global patterns, we then make global maps of LBH emissions for a particular time from instantaneous LBH emission observations. We finally relate global LBH emission maps to the energy flux using a neural network model trained with data from another DMSP instrument that measures the energy flux of precipitating particles as well as LBH emission data. Our study serves as a blueprint for a future comprehensive data-driven modeling of auroral energy flux from ultraviolet imagers onboard LEO satellites.

1. Introduction

As energetic electrons, protons, and photons are deposited into the high-latitude upper atmosphere, their deposited energy begins cascades of energy and interactions that excite and ionize atmospheric oxygen and nitrogen species. This molecular and atomic ionization and dissociation processes result in emissions in the visible, ultraviolet, and extreme-ultraviolet spectra called the aurora. Being able to understand the Earth's aurora provides great insight into physical mechanisms behind the coupling among the magnetosphere, ionosphere, and thermosphere (MIT), and the interactions of this coupled MIT system with the solar wind. Simultaneous global observations of the aurora over the high-latitude region achieved in the past with space-based instruments have proved essential to these efforts. Examples of these instruments include far ultraviolet (FUV) imagers on board spacecraft with highly elliptical near-polar orbits such as the NASA IMAGE and POLAR satellites (Burch et al., 2001; Germany et al., 1998). However, since the deactivation of POLAR in 2008 and loss of contact with IMAGE in 2005, our global observing capabilities of aurora have since been lost. As a result, our space-based coverage of the polar

Project Administration: T. Matsuo
Resources: T. Matsuo
Software: J. Li, L. M. Kilcommons
Supervision: T. Matsuo, L. M. Kilcommons
Validation: J. Li
Visualization: J. Li
Writing – original draft: J. Li
Writing – review & editing: T. Matsuo, L. M. Kilcommons

region is limited to more recently active imagers operating from satellites in low Earth orbit (LEO). Two of these FUV imagers are the GUVI instrument on the TIMED spacecraft (Christensen et al., 2003) and the SSUSI instruments on the DMSP satellite constellation (Paxton et al., 2002). Due to the relatively low altitude of the satellites and improved data link capabilities, these currently operating imagers produce significantly higher spatial resolution than the past imagers but can only provide partial disk coverage. SSUSI's deployment on multiple DMSP spacecraft allows for a greater frequency of observations across multiple tracks in the polar region. As a result, SSUSI's current catalog of more than a decade of FUV emission data can play a role in both quantitatively and qualitatively describing auroral processes. Scientific pursuits to better understand global auroral dynamics, substorm surges, hemispheric asymmetry and dawn-dusk asymmetry of the aurora culminate in ongoing desires to improve the usage of currently available observations of aurora, which is a driving motivation of this study.

Understanding the inter-hemispheric symmetry and asymmetry of the aurora, for instance, requires simultaneous multi-scale knowledge of aurora for both hemispheres. While the assumption of hemispheric symmetry can allow for greater observational coverage over the high-latitude region, recent studies on dayside auroral energy flux using TIMED-GUVI data have shown asymmetries of the dayside aurora morphology due to differences in solar insolation (Liou & Mitchell, 2020a, 2020b). It is also known that the impact of the interplanetary magnetic field (IMF) orientation, especially B_Y component, and dipole tilt angle on MIT coupling often results in the hemispheric asymmetry of the aurora, for example, using ultraviolet images taken from IMAGE and POLAR spacecraft in highly elliptical orbits (Fillingim et al., 2005; Østgaard et al., 2005). Other studies that have taken advantage of the wider spatial coverage provided by space-based ultraviolet imager data include investigations of the dynamical evolution of dayside-nightside and dawn-dusk asymmetries association with auroral substorms. For example, the expansion phase of auroral substorms is characterized by increased intensity of the equatorward boundary of the auroral oval followed by a rapid breakup and poleward motion of auroral arcs on the nightside (Akasofu, 1964). Imager data can also help us to study transient effects such as interplanetary shocks and their impact on auroral morphology. Features associated with the dayside shock aurora are particularly difficult to observe since observations must be made near local noon during the event time interval of approximately 15 min from shock arrival (Zhou et al., 2009). To study these phenomena, Liou and Mitchell (2020a) used global space-based POLAR ultraviolet image data, while Zhou et al. (2009) used ground-based all-sky imager data. To better understand the energy spectrum of particle precipitation associated with shock auroras, the use of in-situ measurements from the FAST and DMSP satellites has been shown to be critical (Zhou et al., 2003).

Despite the benefits of aurora imaging, in-situ instruments such as the Special Sensor J (SSJ) instrument on the DMSP satellite constellation (Redmon et al., 2017), MPA instrument on the LANL satellites (Sicard-Piet et al., 2008), and MEPED on NOAA POES (Asikainen & Mursula, 2013) are required to directly measure the energy spectrum of incident energetic particles. Information about electron-volt energy carried by precipitating energetic electrons and protons is necessary to understand the magnetospheric processes responsible for aurora and compute auroral ionization profiles for modeling thermosphere and ionosphere responses to the aurora. In fact, currently, existing models of auroral energy flux are primarily reliant on auroral flux measurements by in-situ measurements (Hardy et al., 1989; Newell et al., 2009, 2014; Spiro et al., 1982). Used by both NOAA and the Air Force, the Ovation Prime model (Newell et al., 2009, 2014) has been the de facto standard for forecasting the diffuse, monoenergetic, broadband, and proton auroras. While the model is built from observations from the SSJ version 4 (SSJ/4) and version 5 (SSJ/5) instruments on board DMSP satellites, the Ovation Prime model is driven by an empirical function proportional to the dayside magnetic merging rate that can be computed from solar wind data (Newell et al., 2009). Its newer version extends spatial coverage with the inclusion of FUV data from the GUVI instrument by inverting FUV observations using physics-based flux transport models (Newell et al., 2014). Specifically, FUV emissions in the Lyman-Birge-Hopfield (LBH) band are of primary interest for determining energy flux parameters, such as the mean energy and total energy flux. These emissions occur in the 140–180 nm range after excitation of molecular nitrogen (N2). Examples of physics-based models used include Global Airglow (GLOW) model (Solomon, 2017), Boltzmann 3-Constituent (B3C; Strickland et al. [1993]), and Atmospheric Ultraviolet Radiance Integrated Code (AURIC; Strickland et al., 1999). The B3C and AURIC models are used to estimate the auroral energy flux from GUVI data in the Ovation Prime model (Newell et al., 2014), and the B3C model is used to produce the SSUSI Auroral Environmental Data Records (EDR) products from SSUSI data (Johns Hopkins University Applied Physics Laboratory SSUSI Team, 2013). Rigorous inverse modeling involving the GLOW, B3C, and AURIC models are complex and computationally costly, so pre-computed look-up tables are used in the retrieval process. For example, with the help of lookup tables

generated from the B3C electron and ion transport model, the operational algorithm used for SSUSI Auroral EDR data products relates the ratio of LBHL (165–180 nm) and LBHS (140–150 nm) emissions to the mean energy of auroral energy flux and LBHL emission intensity to the total energy. In contrast to the physics-based inversion approach, empirical approaches can be advantageous because of lower initial computational costs and the elimination of errors introduced by inadequate physical assumptions about the ionosphere and thermosphere system. Empirical approaches have often relied on a statistical linear relationship estimated from coincident data between the SSJ and SSUSI instruments in the past (Sotirelis et al., 2013). (The empirical model of Sotirelis et al. (2013) is referred to as S13 later in the paper). The work by R. M. McGranaghan et al. (2021) has produced a new model of total electron energy flux from a combination of DMSP SSJ data and solar wind parameters that achieves a 50% reduction in errors compared to OVATION Prime. Additionally, the work by Robinson et al. (2018) has derived auroral energy flux based on statistical relationships between field-aligned currents and LBH emissions.

While the Ovation Prime model provides statistical maps for four different types of aurora, it is not designed to ingest instantaneous observations like data assimilative procedures such as Assimilative Mapping of Ionospheric Electrodynamics (AMIE; Richmond & Kamide [1988]) and its recent extension Assimilative Mapping of Geospace Observations (AMGeO; Matsuo [2020]). Lu (2017) provides an overview of applications of AMIE procedure for global predictions of ionospheric conductance using SSJ in-situ particle and inferred auroral mean energy and total flux parameters from the POLAR imager data. The use of the Robinson et al. (1987) empirical relationship between auroral flux parameters to conductance is adopted in both AMIE and AMGeO procedures. Assimilative mappings of Hall and Pedersen conductance created using pseudo conductance observations from the SSJ instruments using GLOW by R. McGranaghan et al. (2015); R. McGranaghan et al. (2016) overcome the limiting assumption of the Maxwellian auroral particle distribution. However, none of these assimilative mappings are equipped to use FUV imager data directly. To expand upon the previous assimilative mapping approaches, this work takes advantage of recent developments in machine learning to incorporate a capability to predict auroral energy flux from LBH emission so that FUV imager data can be directly ingested into global assimilative mapping procedures.

With the recognition of the limitations of current space-based in-situ and remote sensing observing systems for auroral energy flux, we present a blueprint for an end-to-end, data-driven modeling approach that enables assimilative mapping of auroral energy flux from space-based FUV images. Given important roles played by global space-based FUV images and global empirical models of auroral energy flux in addressing outstanding science questions in MIT coupling, this work is expected to contribute to extending scientific return from space-based observations of the aurora by the DMSP constellation. We demonstrate the feasibility of this new approach with a prototype developed using the DMSP F16, F17, and F18 SSUSI and SSJ data for the period of February 17th through the 23rd of 2014. The paper is structured as follows: Section 2 presents the preprocessing of the SSJ and SSUSI products used, Section 3 outlines a roadmap for three data analysis methods used for this prototyping approach with methodological details given in subsections, Section 4 presents the results from these methods, Section 5 describes use case of this prototype method, and Section 6 discusses the limitations of the modeling approach.

2. Data Selection and Preprocessing

In this section, we begin with a brief overview of geophysical conditions of the time frame selected for prototyping and demonstration of the approach (Section 2.1). We then describe several preprocessing steps required for in-situ observations of auroral particle precipitation from the SSJ instrument (Section 2.2) and remote-sensing observations of far ultraviolet emissions from the SSUSI instrument (Section 2.3) as well as analysis of spatial-temporal conjunctions between these two types of observations (Section 2.4).

2.1. Geophysical Conditions for 17 February 2014–23 February 2014

Figure 1 presents the time series of the Auroral Electrojet (AE), Disturbance Storm Time (DST), and NASA OMNIWeb SYM-H indices as well as the Interplanetary Magnetic Field (IMF) components By and Bz for this week-long period of February 17th to 23 February 2014. This period was selected for its wide range of geophysical conditions. A series of Earth-directed coronal mass ejections launched starting on February 16th, creating three interplanetary shocks which resulted in three geomagnetic storms suggested in DST and SYM-H indices
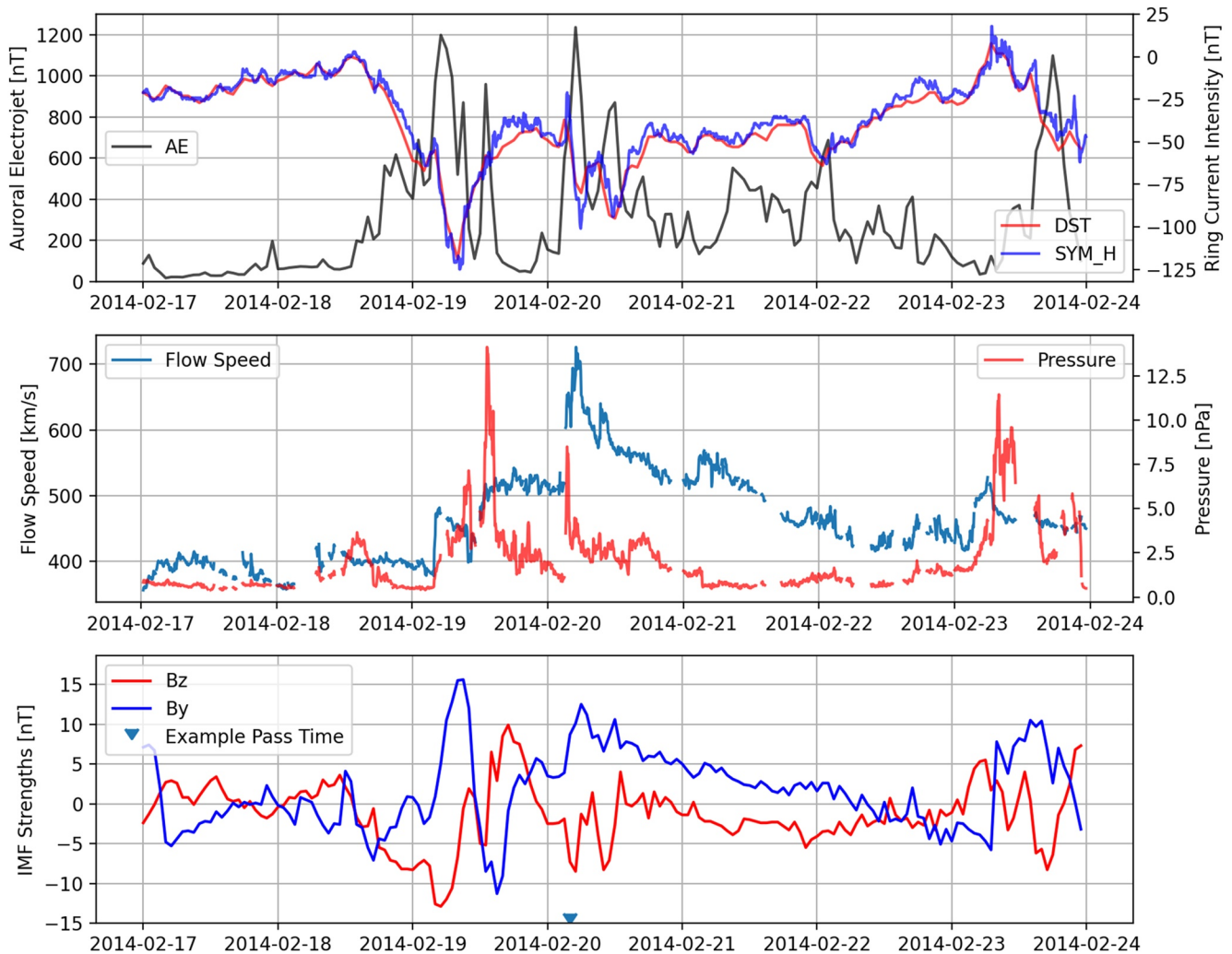
Figure 1. Geophysical conditions during the study period of February 17th to 23rd, 2014. Top: Auroral Electrojet (AE), Disturbance Storm Time, and SYMH Indices. Middle: Solar wind speed and pressure. Bottom: interplanetary magnetic field By and Bz Components in GSM Coordinates. Three major spikes in the AE index correspond to three geomagnetic storms. The triangle mark in the bottom plot denotes an example pass time which is the center time of the Northern Hemispheric pass by DMSP F17 at February 20th 4:02 UTC. Results at this example pass time are presented in Figures 2, 6, 8 and 12.

(Durgonics et al., 2017; Ghamry et al., 2016). The three storms are accompanied by strong auroral electrojet as indicated by AE index and auroral emissions as seen in SSUSI LBH emission data. This time period is also one of the events selected by the Coupling, Energetics and Dynamics of Atmospheric Regions Grand Challenge multi-scale ionosphere-thermosphere system dynamics.

2.2. SSJ

The study uses in-situ observations of particle precipitation from the SSJ/5 instrument on board the DMSP F16, F17, and F18 satellites in magnetic coordinates available from the NASA CDAWeb. These instruments are single triquadraspheric electrostatic analyzers that achieve a total field of view of 4° by 90° (Hardy et al., 2008). The SSJ/5 instrument observes electron and ion flux from particle collision counts across the instrument's 20 logarithmically distributed energy channels (energy range: 30 eV to 30 keV. These observations occur at a temporal resolution of one per second cadence which corresponds to a spatial resolution of approximately 0.1°. These 20-channel energy flux measurements are then integrated to yield electron total energy flux and ion total energy flux values following the processing detailed in (Redmon et al., 2017). Following the notation of Hardy et al. (2008), these electron and ion total energy flux observations are denoted as J_E and J_I, respectively. As our focus is to
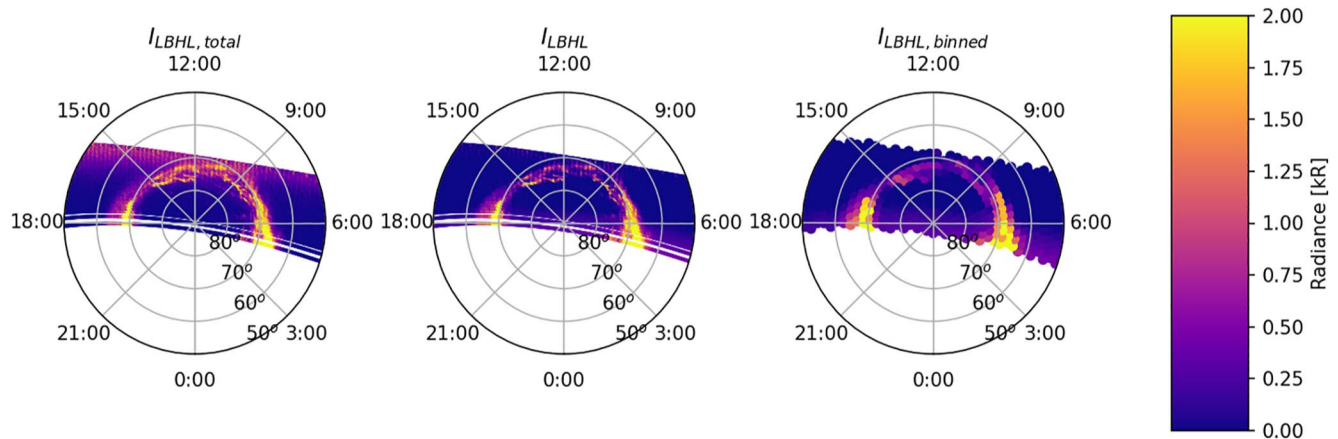
Figure 2. SSUSI SDR LBHL emissions for the Northern Hemispheric pass by DMSP F17 February 20th 4:02 UTC. For all dial plots shown in the Apex geomagnetic coordinates, the dynamic range is 0–2 kilorayleighs with darker colors indicating smaller radiance. Left: High-resolution LBHL radiance given by SSUSI SDR product ($I_{LBHL, total}$). Center: High-resolution LBHL radiance with solar influence removal (I_{LBHL}). Right: Binned LBHL radiance with solar influence removal and spatial averaging ($I_{LBHL, binned}$).

build a global mapping of electron total energy flux in the auroral region, we have used observations poleward of $|50°|$ degrees magnetic latitude. These electron and ion total energy flux values (J_E and J_I) are used to determine a relationship between LBH emissions and electron total energy flux in Section 3.3.

2.3. SSUSI

The SSUSI instrument records FUV radiance images as cross-track swaths occurring every 22 s, with simultaneous sampling in the along-track direction. Under normal operation, the SSUSI instrument records FUV emissions in terms of light intensities across 5 wavelength bands or "colors". The two colors that relate to LBH emissions, the LBHS band spanning wavelengths of 140–150 nm and LBHL band spanning wavelengths of 165–180 nm, are used. Observations of LBH emissions used in the study are taken from the version 0116 SSUSI SDR data product from the NASA CDAweb. In the SDR product used, these LBH radiance measurements are adjusted to be what would be seen if the same piercepoint locations (where a line of sight of measured radiance intersects a ionospheric shell) were observed from directly overhead (Johns Hopkins University Applied Physics Laboratory SSUSI Team, 2013). This process of accommodating for observation look angle is called rectification. LBH emission observation locations and times are taken from the auroral piercepoint measurements and LBH emissions are taken from the high resolution disk rectified intensity auroral measurements. The auroral piercepoint measurement locations given in terms of geographic latitude and longitude in the SDR product are then converted to magnetic latitude and longitude using Apex geomagnetic coordinates (Richmond, 1995) at a reference altitude of 110 km. As with the SSJ observations, only observations poleward of $|50°|$ magnetic latitude are used.

2.3.1. Removal of Solar Influence

The FUV radiances contained in the SSUSI SDR data product are high-resolution and can be generated by both solar illumination and auroral particle precipitation. The total radiance values in the LBHL and LBHS band are denoted as $I_{LBHL, total}$ and $I_{LBHS, total}$, respectively, while the auroral contribution are denoted as I_{LBHL} and I_{LBHS}, respectively. See an example of the total LBHL emission $I_{LBHL, total}$ from the high-resolution SSUSI SDR product, shown in the left plot of Figure 2 in magnetic coordinates, for a Northern Hemisphere high-latitude pass by DMSP F17 during the UTC 3:49 to 5:31 on February 17th. This subsection describes a preprocessing step applied to $I_{LBHL, total}$ and $I_{LBHS, total}$ to isolate LBH emissions I_{LBHL} and I_{LBHS} due to auroral particle precipitation. Note that this SSUSI data preprocessing is done at high resolution, and I_{LBHL} and I_{LBHS} are the same resolution as the SSUSI SDR data products.

To isolate the auroral contribution from the solar contribution in the SSUSI LBH emission data, methods from (Robinson et al., 2018) are used. By linearly fitting the total LBH radiances to the cosine of the solar zenith angle of the observation locations, an approximate model can be made for the solar influence as follows.

$$I_{LBHL} = I_{LBHL,Total} - I_{LBHL,Solar}$$

$$I_{LBHL,Solar} = A_L \cos(\Psi) + b_L$$

<div align="right">(1)</div>

where Ψ is the solar zenith angle and $I_{LBHL, Solar}$ is the solar contribution to the total LBHL radiance measured by SSUSI, $I_{LBHL, total}$. A_L and b_L are constants determined through least squares linear fitting on a set of SSUSI LBHL emission data. The solar contribution to the LBHL data is then subtracted from the total LBHL radiance $I_{LBHL, Total}$ to yield the auroral LBHL radiance I_{LBHL}. For each hemispheric pass, the coefficients A_L and b_L are refitted to determine the solar influence on that particular pass. If the subtraction of the solar contribution results in a negative value, I_{LBHL} is set to 0. See the middle plot of Figure 2 for an example of the I_{LBHL} calculated from $I_{LBHL, Total}$ for a DMSP F17 pass during the UTC 3:49 to 5:31 on February 17th. This process is repeated for the total LBHS radiance to determine the auroral LBHS emission I_{LBHS}. For the remainder of this paper, these preprocessed data I_{LBHL} and I_{LBHS} are referred to as LBHL and LBHS emission data. I_{LBHL} and I_{LBHS} data are then used in neural network analysis described in Section 3.3.

2.3.2. Spatial Binning and Averaging

Spatial binning and averaging the preprocessed data (with the solar irradiance removed) facilitate assimilative mapping and principal component analysis of LBH emission data I_{LBHL} and I_{LBHS}, using the polar-cap spherical harmonics basis functions developed for the AMIE (Richmond & Kamide, 1988) and used in the AMGeO (Matsuo, 2020), as described in Sections 3.2 and 3.1. This preprocessing also makes overall computational cost manageable. Note that fine-scale features visible in the high-resolution SDR data product, that are averaged out by this spatial binning process, cannot be captured with the adopted basis functions at the spherical harmonics degree and order of about 72 and 12, corresponding to the resolution of 2.5° in latitude and 15° in longitude.

I_{LBHL} and I_{LBHS} obtained from preprocessing described in Section 2.3.1 are here spatially binned using equal area binning, with a constant bin width of 2° in latitude, but variable width in the longitude to approximate equal surface area for each bin. For each spatial bin of I_{LBHL} data, a mean value is used as the representative radiance value for that spatial bin $I_{LBHL, binned}$ and a variance value with respect to the mean is computed. This process is repeated for I_{LBHS} to yield $I_{LBHS, binned}$. The effect of spatial binning and averaging can be seen in the middle and right plots of Figure 2 where the number of LBHL emission data points are reduced from 14,085 to 456. These spatially binned LBH data, $I_{LBHL, binned}$ and $I_{LBHS, binned}$, are then used in assimilative mapping and principal component analysis described in Sections 3.1 and 3.2.

2.4. SSUSI and SSJ Conjunctions

In order to establish a quantitative relationship between electron total energy flux and LBH emissions using neural network analysis described in Section 3.3, a training data set is required. SSUSI LBHL and LBHS emission I_{LBHL} and I_{LBHS} data and SSJ electron and ion energy flux J_E and J_I data need to be paired as input and supervisory (output) data. Due to the spatial-temporal sampling mismatch between the SSUSI LBH imager and SSJ particle precipitation instrument, several steps are required to determine the SSUSI-SSJ conjunction.

Since the resolution of LBH emission observations or "pixels" in the SSUSI SDR data product is considerably higher than a spatial sampling of the SSJ particle precipitation observations, the first step in determining SSUSI-SSJ conjunctions is finding the nearest SSUSI "pixels" to each SSJ observation point and applying spatial smoothing to obtain SSUSI LBH conjunction values. This spatial smoothing contributes to an enhancement of the image structures through effective signal-to-noise improvement. With k as a positive integer, the ball-tree data structure (Omohundro, 1989) implemented in Sklearn's nearest neighbors functions, is used to computationally efficiently determine the nearest k SSUSI I_{LBHL} "pixels" to a given SSJ observation point. A representative value of I_{LBHL} in conjunction with the SSJ observation is then computed as the distance weighted average of these SSUSI nearest neighbors. This conjunction value denoted as $I_{LBHL, smoothed}$ is computed as

$$I_{LBHL,smoothed} = \sum_{i=1}^{k} w_i I_{LBHL,i}$$
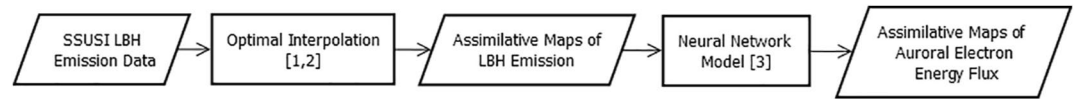
<div align="right">(2)</div>

Figure 3. Flowchart describing how SSUSI LBH emission data are transformed to global assimilative maps of auroral electron energy flux by a combination of three data-driven modeling approaches. [2] The OI, which incorporates [1] EOF analysis results, generates assimilative maps of global LBH emission from SSUSI LBH data. Using [3] the pre-trained neural network predictive model of auoral electron energy flux, global maps of LBH emission are transformed into global maps of auroral electron energy flux.

where SSUSI LBH emission at a given "pixel" is denoted by $I_{LBHL,i}$, the corresponding weights of each pixel's contribution, w_i, is set to be inversely proportional to the great circle (Haversine) distance between the SSJ observation point and SSUSI pixel locations. These weight terms are then scaled such that their sum equals 1. For each of the SSJ observations, the nearest 10 pixels ($k = 10$) contributed to the SSUSI conjunction value, $I_{LBHL, smoothed}$.

This process is repeated to retrieve LBHS conjunction data ($I_{LBHS, smoothed}$). Since the SSUSI instrument records its images one cross-track swath at a time, this implies there is a slight temporal difference between the 10 pixels across track. However, the effect of this slight temporal lag is negligible compared to the 25 km spatial binning adopted in the production the SSUSI SDR product data. Overall, this distance weighted averaging is a robust methodology for providing spatial conjunction data between SSUSI and SSJ observations.

Strictly speaking, SSUSI points directly downward of the DMSP spacecraft once per sweep while in-situ SSJ sampling occurs every second, which may introduce up to about 20 s spatiotemporal mismatch between any pairs of SSUSI and SSJ observations. To account for such discrepancy, smoothing is also applied to SSJ electron and ion energy flux J_E and J_I data to yield $J_{E,smoothed}$ and $J_{I,smoothed}$. Smoothing of the SSJ electron and ion total energy flux values are accomplished by taking the running mean of 10 consecutive observation points for each hemispheric DMSP pass using the uniform filter1d function implemented in SciPy. This value of 10 consecutive observation points was chosen to roughly match the resolution of the SSUSI data used. Smoothing also helps reduce the impact of single particle events that result from particles with energies greatly exceeding the SSJ instrument's maximum detectable energy of 30 keV. The interaction of this highly energized particle with the sensor materials results in strong particle flux across all detector channels. The use of smoothed SSJ electron and ion energy flux $J_{E,smoothed}$ and $J_{I,smoothed}$ in neural network analysis described in Section 3.3 thus allows supervisory learning from higher signal-to-noise data sets.

3. Data-Driven Auroral Modeling Approach

To develop a new assimilative mapping procedure of global auroral electron energy flux for SSUSI LBH emission data, three data analysis methods are combined. As shown in the flowchart displayed in Figure 3, this procedure is designed to take SSUSI LBH emission data as sole input and transform into global assimilative maps of auroral electron energy flux through a combination of the following approaches: (a) Empirical Orthogonal Function (EOF) analysis described in Section 3.1, (b) assimilative mapping analysis using Optimal Interpolation (OI) described in Section 3.2, and (c) neural network modeling to predict auroral electron energy flux from LBH emission as described in Section 3.3.

3.1. Empirical Orthogonal Function (EOF) Analysis of LBH Emission

EOF analysis facilitates modeling the background model error covariance required in the OI; a vital step toward the development of assimilative maps of LBH emission. EOFs are a set of empirically-determined orthogonal functions that represent dominant eigenmodes of variability in LBH emission changes. Due to the spatially sparse and temporally irregular LBHL and LBHS emission data, we cannot use a conventional eigenvalue decomposition approach to EOF analysis or principal component analysis that relies on factorization of a sample covariance obtained from complete data sets. Instead, a sequential nonlinear regression analysis is used to determine EOFs from incomplete SSUSI data sets following the methods of Matsuo et al. (2002).

A key part of this alternate EOF approach is to reduce the effect of incomplete data by representing the EOFs using the polar-cap spherical harmonics basis functions developed for the AMIE (Richmond & Kamide, 1988)

and used in the AMGeO (Matsuo, 2020). In the rest of the paper, we represent the basis functions as $\mathbf{X}(r)$, where r represents the spatial position in magnetic latitude and magnetic local time. EOFs are then expressed as a sum of these basis functions, $\mathbf{X}\boldsymbol{\beta}$, where columns of $\boldsymbol{\beta}$ are vectors of polar-cap spherical harmonic coefficients for the vth EOF $\boldsymbol{\beta}^{(v)}$. If y' is the residual SSUSI LBH binned observations $I_{LBHL,\,binned}$ and $I_{LBHS,\,binned}$ after removal of the mean at the location r and median time t of a given satellite high-latitude overpass, then y' is decomposed as

$$y'(r,t) = \alpha^{(1)}(t)\mathbf{X}(r)\boldsymbol{\beta}^{(1)} + \cdots + \alpha^{(v)}(t)\mathbf{X}(r)\boldsymbol{\beta}^{(v)} + e'(r,t) \tag{3}$$

where α represents the time-dependent scaling of the vth EOF, and e' represents the residual observations after removing the mean and scaled EOF contributions. Sets of these α and β coefficients are determined as in Matsuo et al. (2002) wherein the QR method (or Gram-Schmidt method) is used to orthogonalize the vectors of harmonic coefficients $\beta^{(v)}$. Once $\beta^{(v-1)}$ is estimated, subsequent orthogonal directions $\beta^{(v)}$ are estimated using residual data. This process is then repeated to estimate two sets of eight EOFs from $I_{LBHL,\,binned}$ and $I_{LBHS,\,binned}$ data. All preprocessible SSUSI data from DMSP F16, F17, and F18 across both hemispheres during the week period was used.

To prevent nonphysical features arising from regression analysis of spatially sparse data using the polar-cap spherical harmonics, harmonic coefficients $\beta^{(v)}$ are regularized using the L2 norm (Tikhonov regularization) via Ridge regression as implemented in Scikit-Learn (Rifkin & Lippert, 2007). Here the objective function minimized during the sequential nonlinear regression analysis has an additional penalty term as shown below,

$$L(\beta) = \sum_{i=1}^{n}\left(y_i - \sum_{j=1}^{p} x_{ij}\beta_j\right)^2 + \lambda \sum_{j=1}^{p} \beta_j^2 \tag{4}$$

where λ determines the strength of this penalty term, p is the total number of EOFs, and n is the number of observations. The value of λ minimally affects the spatial structure of EOFs, and the unit λ value is used in this work.

3.2. Assimilative Mapping Analysis of LBH Emission Using Optimal Interpolation (OI)

This study uses the assimilative mapping technique described in Richmond and Kamide (1988) and Matsuo et al. (2005) and employed in the AMGeO software package (AMGeO Collaboration, 2019). The same approach, here referred to as the OI, is used in works by Shi et al. (2020), R. McGranaghan et al. (2016), Matsuo et al. (2015), Cousins et al. (2015), and Cousins et al. (2013) and is summarized in Matsuo (2020). The OI technique combines a prior background model and observations using uncertainty information given as the background model error and observation error covariances to produce a posterior mean of assimilative maps according to Bayes' rule. The OI analysis is conducted separately for the SSUSI LBHL and LBHS emissions, at the median time of each satellite hemispheric high-latitude overpass, using SSUSI LBH binned observations $I_{LBHL,\,binned}$ and $I_{LBHS,\,binned}$ from that overpass.

The OI is essentially a non-recursive application of the Kalman filter measurement update. Suppose $\mathbf{y}$ denotes a vector of SSUSI LBHL binned observations $I_{LBHL,\,binned}$ (or LBHS binned observations $I_{LBHS,\,binned}$) at a given OI analysis time, $\mathbf{x_b}$ and $\mathbf{x_a}$ are vectors of the prior and posterior mean of LBHL emission on the AMGeO grid, defined by 24 latitude points and 37 local time points for a total of 888 grid points, and $\mathbf{y_b}$ is the prior spatial prediction of SSUSI LBHL binned observations, the OI analysis $\mathbf{x_a}$ is given using the Kalman measurement update equation as

$$\mathbf{x_a} = \mathbf{x_b} + \mathbf{K}\left(\mathbf{y} - \mathbf{y_b}\right) \tag{5}$$

where $\mathbf{K}$ is a Kalman gain matrix which is a function of the background model error covariance $\mathbf{C_b}$ and the observation error covariance $\mathbf{C_r}$ as given below

$$\mathbf{K} = \frac{\boldsymbol{\rho_{x,y}} \circ \mathbf{C_b}\mathbf{H^T}}{\boldsymbol{\rho_{y,y}} \circ \mathbf{H}\mathbf{C_b}\mathbf{H^T} + \mathbf{C_r}} \tag{6}$$

where $\mathbf{H}$ denotes an interpolation operator that converts the LBHL emission on observation locations to the AMGeO grid, $\boldsymbol{\rho_{x,y}}$ and $\boldsymbol{\rho_{y,y}}$ are the localization correlation matrices specified using kernels developed in (Gaspari

& Cohn, 1999). For this optimal interpolation, the cut off localization distance of 18° is used following a default setting adopted in the AMGeO software. Note that $\mathbf{H}$ is implemented using polar-cap spherical harmonics basis functions $\mathbf{X}$ evaluated at observation locations as explained in (Matsuo, 2020).

For the prior (background model) mean $\mathbf{x_b}$, we chose to use the mean of LBH binned observations $I_{LBHL, binned}$ and $I_{LBHS, binned}$ computed for each satellite overpass as described in Section 2.3.2. Following the approach adopted in (Matsuo et al., 2015), the prior (background model) error covariance $\mathbf{C_b}$ is expressed as a low rank covariance using a set of leading eigenvectors approximated by EOFs as

$$\mathbf{C_b} = \mathbf{\Gamma} < \boldsymbol{\alpha}, \boldsymbol{\alpha}^T > \mathbf{\Gamma}^T \tag{7}$$

where $\mathbf{\Gamma}$ is a matrix with 8 columns filled leading EOFs estimated from Section 3.1 and $\boldsymbol{\alpha}$ is a vector of the time-dependent scaling coefficients of EOFs. The EOF coefficient covariance $< \boldsymbol{\alpha}, \boldsymbol{\alpha}^T >$ is approximated as a diagonal matrix using a sample variance computed from a time-series of $\hat{\boldsymbol{\alpha}}(t)$ estimated from the EOF analysis described in Section 3.1. Note $\mathbf{\Gamma} = \mathbf{X_g}\hat{\boldsymbol{\beta}}$ where $\mathbf{X_g}$ is the polar cap spherical harmonics basis functions $\mathbf{X}(r = r_g)$ evaluated on the AMGeO grid and $\hat{\boldsymbol{\beta}}$ is a vector of harmonics coefficients estimated in Section 3.1.

The observation error covariance $\mathbf{C_r}$ is represented by a diagonal matrix with the assumption that errors of SSUSI LBHL binned observations $I_{LBHL, binned}$ (or LBHS binned observations $I_{LBHS, binned}$) are uncorrelated. Although uncertainties are provided with the SSUSI SDR data product for both LBHL and LBHS emissions, it is not clear how they can be propagated through the prepossessing steps described in Sections 2.3.1 and 2.3.2. Instead observational error covariances $\mathbf{C_r}$ for $I_{LBHL, binned}$ and $I_{LBHS, binned}$ are specified using the variance of the observations in each spatial bin as described in Section 2.3.2.

3.3. Neural Network Predictive Modeling of Auroral Energy Flux From LBH Emission

We leverage the flexibility of neutral network modeling to learn nonlinear complex relationships between electron total energy flux using LBH emissions from SSUSI-SSJ conjunction data described in Section 2.4. After applying feature selection and engineering steps to $I_{LBHL, smoothed}$, $I_{LBHS, smoothed}$, $J_{E,smoothed}$, and $J_{I,smoothed}$ as described in Section 3.3.1, Section 3.3.2 shows how a simple feedforward neural network, based off the artificial neural network originally described by McCulloch and Pitts (1943), is used for the machine learning of an auroral energy flux predictive model.

3.3.1. Feature Selection and Engineering

The neural network model is learned from three input feature data sets consisting of $I_{LBHL, smooth}$, $I_{LBHS, smooth}$, and ion energy flux activity mask derived from $J_{I,smoothed}$, and the supervisory (output) data set of $J_{E,smoothed}$. Since LBH radiances produced by electron and ion precipitation are additive (Knight & Strickland, 2013), the use of the third input feature of ion energy flux activity mask helps account for the ion contributions to LBH emission. For example, Sotirelis et al. (2013) excluded SSUSI-SSJ conjunction data in fitting of a linear model when the ratio between electron and ion flux exceeded a certain threshold. Following a similar vein, this third, binary input is based on the preprocessed in-situ SSJ measurements of ion energy flux $J_{I,smoothed}$. This binary feature input, M_I, takes on a value of one whenever the ion energy flux is sufficiently high and otherwise zero as described below.

$$M_I = \begin{cases} 1, & \text{if } J_{I,smoothed} > 0.1 \, \dfrac{ergs}{cm^2 \cdot s \cdot sr} \\ 0, & \text{otherwise} \end{cases} \tag{8}$$

where an absolute cut-off threshold value of $0.1 \, \frac{ergs}{cm^2 \cdot s \cdot sr}$ is set through the trial and error calibration based on the neutral network performance. To facilitate neural network training, $I_{LBHL, smooth}$, $I_{LBHS, smooth}$, and $J_{E,smoothed}$ are further scaled and normalized. Scaling and normalizing is often done to speed up the gradient descent algorithm employed when estimating weights. The distribution of $I_{LBHL, smooth}$, $I_{LBHS, smooth}$, and $J_{E,smoothed}$ data suggests a heavy-tailed data sample distribution with the presence of fairly high positive skewness. With such a distribution, standard normalization techniques, which involve removal of the mean and scaling to unit variance, are not
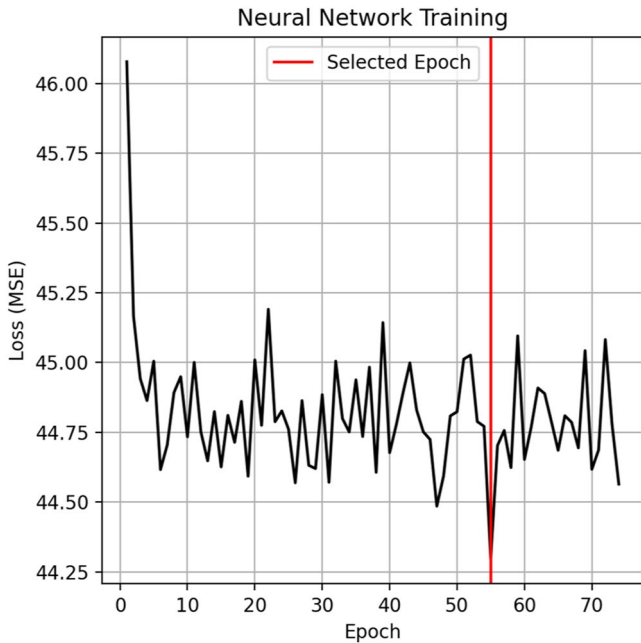
Figure 4. The mean squared error (MSE) loss functions after each training epoch. Note the MSE value shown here does not correspond to true physical units due to the use of scaled and normalized inputs. The vertical red line denotes the epoch of minimum loss.

recommended since these techniques are strongly affected by outlier values. Instead, these values are normalized with the removal of the median value and scaled using the interquartile range.

One week's worth of SSUSI-SSJ conjunction data results in 698,000 conjunction points from 580 hemispheric high-latitude satellite passes. Reflecting the impact of geophysical conditions on data sets, the training and test sets are separated by their respective hemispheric passes instead of the more traditional point-by-point approach. In other words, SSUSI-SSJ conjunction data points from one particular hemispheric satellite pass are never separated into both the training and test sets. These hemispheric passes are randomly split into train and test sets with 522 passes used in the training set and 58 used in the testing set.

3.3.2. Neural Network Model Design and Training

Considering there are only three input features with one output, we have opted for a shallower, wider neural network model design with three layers consisting of an input layer, one hidden layer, and an output layer. The input layer takes in scaled $I_{LBHL, smooth}$ and $I_{LBHS, smooth}$ as well as M_I as input, and has eight output neurons connected to the second, hidden layer. The second, hidden layer then outputs 8 neurons to the final layer. This hidden layer enables the neural network additional degrees of freedom in the nonlinear transformation of the inputs. For this hidden layer, we use the leaky relu activation function which provides many of the same benefits as the high-performance, traditional relu activation function while also addressing the commonly experienced neuron death issue that can cause the model to be less adaptive to changing inputs (Xu et al., 2015). The final layer then outputs the model prediction for the scaled electron total energy flux $J_{E,smoothed}$. This neural network design led to a total of 41 trainable parameters, and the neural network is implemented using Python Keras 2.4.0.

The neural network model is trained using the Adam optimizer (Kingma & Ba, 2017) which is implemented in Keras 2.4.0 for an epoch limit of 200 epochs using the mean squared error (MSE) as the loss function. The Adam optimizer is chosen as the gradient descent algorithm due to its overall performance and robustness. Upon learning of each model, model parameters such as number of neurons, number of layers, number of training epochs, or hyper-parameters, are calibrated iteratively based on model performance evaluated using the test data set. To ensure optimal stopping of training, early stopping callback conditions are implemented. These callback conditions stipulate that model training should stop if the model performance measured through the MSE loss function does not improve after a certain number of epochs. A stopping buffer of 40 epochs is used in this work. After the last epoch, the model parameters associated with an epoch with the lowest loss function value is chosen for the final model. Figure 4 displays how the MSE loss function varies across the epochs of the neural network training. After the first 10 epochs, the loss function values decrease slowly with increasing epochs with considerable variability which indicates that our model was quickly trained. For our final neural network model, the weights associated with the lowest cost epoch shown by the vertical red line are selected. It is important to note that the MSE value shown in Figure 4 is that of the scaled and normalized outputs.

4. Data Analysis Results

This section summarizes data analysis results from approaches described in Sections 3.1, 3.2, and 3.3. Sections 4.1 and 4.2 present the results from EOF analysis and assimilative mapping analysis of LBH emission data. Section 3.3 describes the prediction performance of the neural network model described in Section 3.3. For this performance assessment, the auroral electron energy flux is compared to LBH emission on a satellite track pass-by-pass basis.
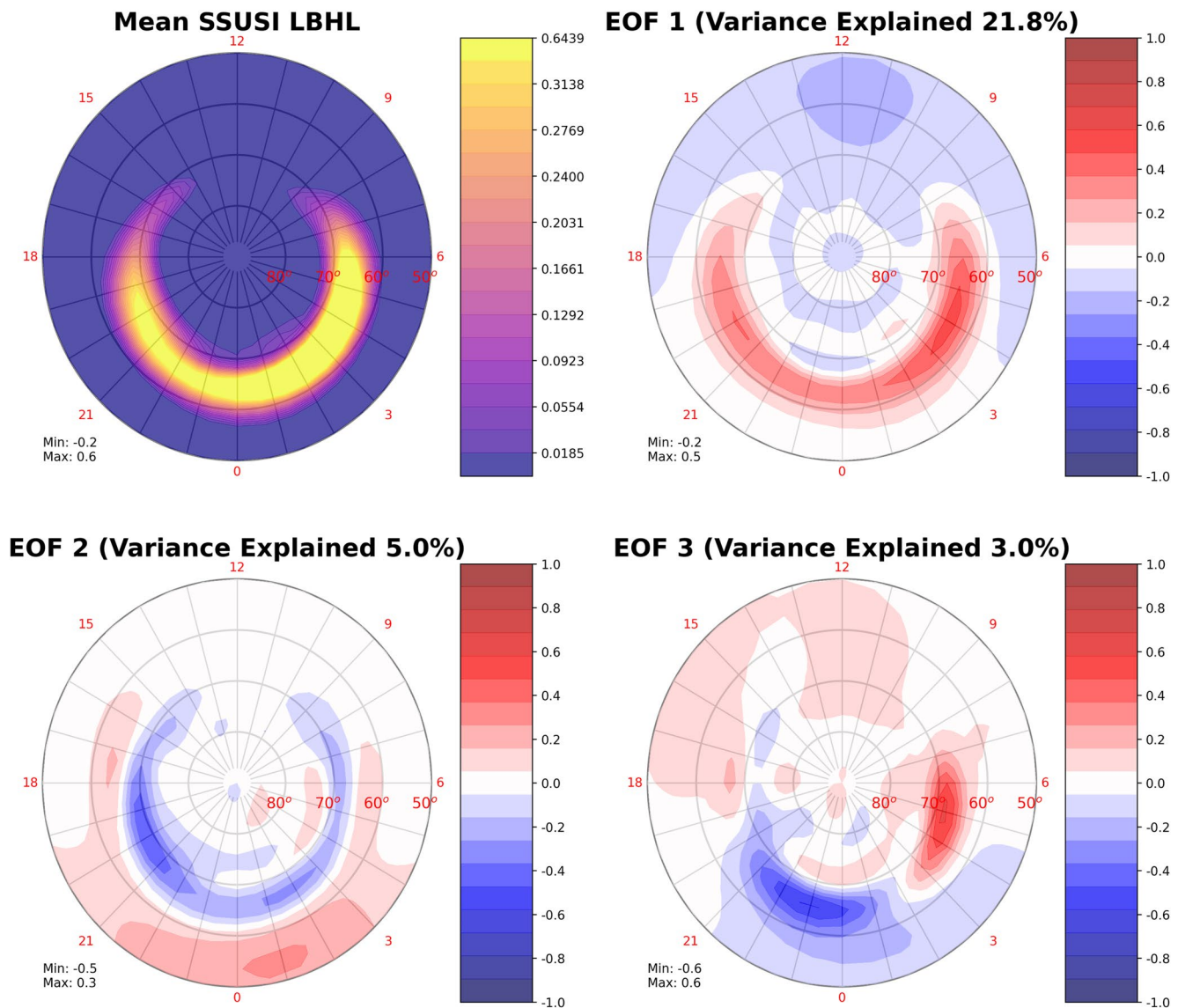
Figure 5. Global patterns of the mean and three dominant modes for LBHL emission variability estimated from preprocessed SSUSI LBHL emission data over February 17-23 2014. The mean pattern (top left) is shown in terms of photon flux in kilorayleigh. The EOF patterns are unit-less and normalized.

Table 1
The Variance in LBHL Emission Explained by the Leading 8 EOFs

EOF #	% Variability explained	% Cumulative variability
EOF 1	21.8	21.8
EOF 2	5.0	26.8
EOF 3	3.0	29.8
EOF 4	1.9	31.7
EOF 5	2.0	33.7
EOF 6	1.5	35.2
EOF 7	1.4	36.6
EOF 8	1.0	37.6

4.1. Global Modes of LBH Emission Variability

Because LBHL emission intensity is proportional to the total electron energy flux, this section focuses on the global modes of LBHL emission variability derived from preprocessed SSUSI LBHL emission data $I_{LBHL, binned}$. The results from LBHS emission data and $I_{LBHS, binned}$ can be found in Supporting Information S1. Figure 5 shows the mean and three dominant modes of LBHL emission variability over February 17-23 2014. The mean pattern reflects a typical auroral oval with a stronger post-midnight emission, which appears similar to the diffuse auroral patterns found in other global auroral models such as the Ovation Prime (Newell et al., 2014). This mean pattern is also similar to the Hall and Pedersen conductance mean patterns associated with EOF analysis by R. McGranaghan et al. (2015) but shifted counter clockwise by a few hours. Table 1 shows the percentage variability explained by each mode along with the cumulative percentage. Overall this set of eight

Table 2
Pearson Correlations of $\hat{\alpha}$ With IMF and Geomagnetic Indices

EOF	AE index	AL index	By (GSM)	Bz (GSM)
1	0.836	−0.824	0.407	−0.532
2	−0.197	0.181	0.211	0.173
3	−0.014	0.032	0.031	−0.219

EOFs explains 37.6% of the observed variance from the mean of LBH emission with the first three modes being responsible for 29.8%. Most leading modes associated with the higher variance contribution exhibit large-scale features, while high-order modes are typically composed of much smaller spatial scale features. To facilitate geophysical interpretation of EOFs, correlations of the time-dependent scaling coefficients of the leading three EOFs $\hat{\alpha}(t)$ with IMF and geomagnetic indices are shown in Table 2. To create a one-to-one time series that matches the irregular EOF analysis time interval t that is set to be the median time of each satellite high-latitude overpass, 30-min running means of IMF and geomagnetic indices are computed using 5-min NASA/GSFC's OMNI data centered at EOF analysis time t. No additional time lagging is done on the NASA/GSFC's OMNI data. Since these EOFs do not necessarily correspond to independent physical processes, each EOF correlates with multiple geophysical parameters.

EOF 1 accounts for 21.8% of the variability from the mean and represents a strengthening and weakening of the typical auroral oval shape as captured by the mean pattern. The amplitude of EOF 1 is strongly correlated with the AE index with a correlation coefficient of 0.84, and EOF 1 is therefore interpreted to represent changes of the overall auroral oval associated with geomagnetic activities. Features on the dayside are unphysical, resulting from the lack of DMSP SSUSI data coverage at the mid latitude noon sector. Our finding on the LBHL EOF 1 is generally consistent with findings of Hall and Pedersen EOF 1 reported in R. McGranaghan et al. (2015), with a slightly higher correlation of LBHL EOF 1 with the AE index. LBHL EOF 2 accounts for 5% of the variability and can be visually interpreted as an equatorward expansion and poleward contraction of the auroral oval that is mostly dawn-dusk symmetric. The impact of the lack of DMSP SSUSI coverage shows up as unphysical features in the mid latitude night side. This LBHL EOF 2 is similar to the appearance of Hall and Pedersen EOF 2 reported in R. McGranaghan et al. (2015) with a stronger feature on the high latitude dusk area. EOF 3 accounts for only 3% of the variability, but it can be speculatively described as a westward shifting of the auroral oval associated with substorms, introducing a characteristic dawn-dusk asymmetry. This LBHL EOF 3 is also similar to the appearance of Hall and Pedersen EOF 3 reported in R. McGranaghan et al. (2015) with some differences.

The weak correlation of LBHL EOF 2 and EOF 3 with IMF and geomagnetic indices may suggest difficulties to identify these modes only from 1 week of DMSP SSUSI data. Because of the need to take 30-min running means of IMF and geomagnetic indices in these correlation studies to match with the EOF analysis interval, it is challenging to establish a correlation during rapid changes associated with aurora dynamics.
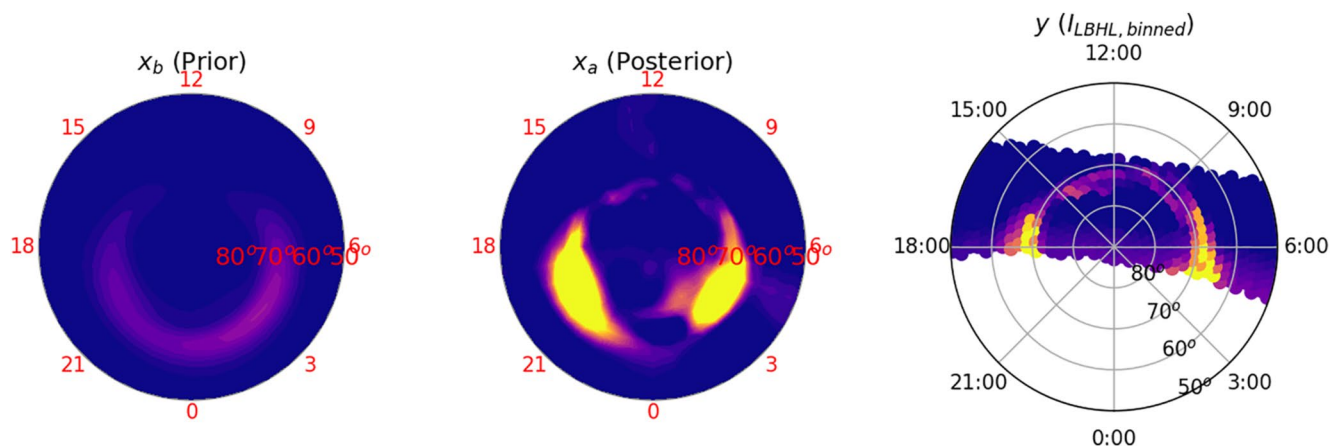

Figure 6. Assimilative mapping of LBHL emissions for the SSUSI pass is indicated in Figure 1. The dynamic range for all subplots is 0–2 kilorayleighs with darker colors indicating smaller radiance in the linear color contour scale defined as the colorbar for Figure 2. Left: Prior State or sample mean of LBHL emissions for the week long frame selected. Middle: Assimilation result of LBHL emission after ingestion of SSUSI LBHL observations shown on the right subplot. Right: The spatially averaged SSUSI LBHL observations fed into the AMGeO procedure taken from the Northern Hemispheric pass by DMSP F17 February 20th 4:02 UTC.

4.2. Assimilative Maps of LBH Emission

Using the OI methodology described in Section 3.2, assimilative maps of both LBHL and LBHS emissions are generated for all 58 hemispheric high-latitude satellite passes from the test data set. As explained in Section 3.3.1, these 58 passes, out of a total of 580 hemispheric high-latitude satellite passes, are set aside from neural network training for testing. The middle plot of Figure 6 presents an assimilative map of LBHL emission for the same satellite pass presented in Figure 2 in the preprocessing Section and Figure 8. The prior mean and observations ingested into the OI are shown on the left and right plots of Figure 6, respectively. The influence of observational noise is likely manifesting as some unphysical features in the dawn region of the assimilative map. More systematic calibrations of the observational error covariance and the covariance localization parameter will likely help mitigate these issues. Future work with a larger data set is expected to improve the quality of background model error covariance modeled with EOFs (see Equation 7) as well as resulting assimilative maps. Figure 7 shows another OI result from DMSP F16 overpass over the Northern Hemisphere on February 22nd at 2:37 UTC, showing a more typical auroral feature with strong features at the dusk sector. This example suggests a promising capability of the OI to reproduce both the discrete and diffuse aurora features.

4.3. Prediction of Auroral Energy Flux From LBH Emission

To evaluate the performance of the trained neural network model to predict out-of-sample electron total energy flux, we use 58 hemispheric polar passes withheld from training. Note that a total of 580 DMSP hemispheric high-latitude satellite passes is randomly divided into training and test sets of 522 and 58 passes as described in Section 3.3.2. For comparison, the prediction by using the S13 linear empirical model of Sotirelis et al. (2013) is shown. Note that the scope of comparison of the neural network model to the S13 model that was developed for a broader range of cases is limited, and intended only to demonstrate the feasibility and potential of the neural network modeling approach prototyped in this study for future large-scale development efforts.

Figure 8 shows the model prediction for a DMSP F17 Northern Hemispheric pass centered at 4:02 UTC on February 20th. This is the same pass shown in Figure 2. The middle plot shows the three inputs (scaled $I_{LBHL, smooth}$ and $I_{LBHS, smooth}$ as well as M_I) into the neural network model. The top plot shows the auroral energy flux prediction output from the neural network model (orange) and the S13 prediction (cyan) along with the auroral electron energy flux from the test set (red). The bottom plot shows the spectrogram of the electron energy fluxes recorded by the SSJ instrument along this pass. For this pass, we see the neural network model and S13 predictions are similar in the sense that both underestimate higher values of observed electron energy flux but follow the overall trend over time. While the neural network model and S13 perform comparably for the hemispheric test pass shown in Figure 8, the hemispheric pass by DMSP 17 19 February 2014 at 2:32 UTC on February 19th shown in Figure 9 demonstrates the limitation of S13. We can see the auroral emission and precipitation signal over this pass have three peaks. The last precipitation peak is not well captured in LBHL emission data which causes the S13 prediction to fail, while the neural network model prediction closely matches the observed auroral electron flux signal. We see here the advantage of the neural network approach to represent a nonlinear complex relationship between input and supervisor (output) data. Figure 10 shows the comparison for another test pass over the Southern Hemisphere by DMSP F16 on February 19th at 8:24 UTC. Here both the neural network and S13 models erroneously predict a high activity region at the beginning of the pass that corresponds to the dusk side of this dawn-dusk DMSP F16 pass. This duskside high activity region most likely results from the impact of high ion flux on LBH emission that is not adequately portrayed by the use of an ion flux activity mask.

The overall model performance is summarized in Tables 3 and 4 to examine the connection to the signal-to-noise ratio of training data at different geomagnetic activity levels. Across the 58 test hemispheric high-latitude satellite passes, the neural network model performs better during high geomagnetic activity when stronger input signals from LBH emission data as indicated by the Pearson correlations between the prediction and test data for AE levels higher or lower that 450 nT summarized in Table 3. The median AE index over the time interval of each pass computed from 5-min AE values is used. During geomagnetically quiet times, it is expected the neural network to have more trouble with distinguishing meaningful signals from noises in traning data sets of $I_{LBHL, smooth}$, $I_{LBHS, smooth}$, and $J_{E,smoothed}$, resulting in poorer performance for test passes with lower AE values. From Table 3, we see that for both high and low geomagnetic activity levels, the neural network model prediction correlates better with observed electron flux than the S13 prediction. This performance difference is even more
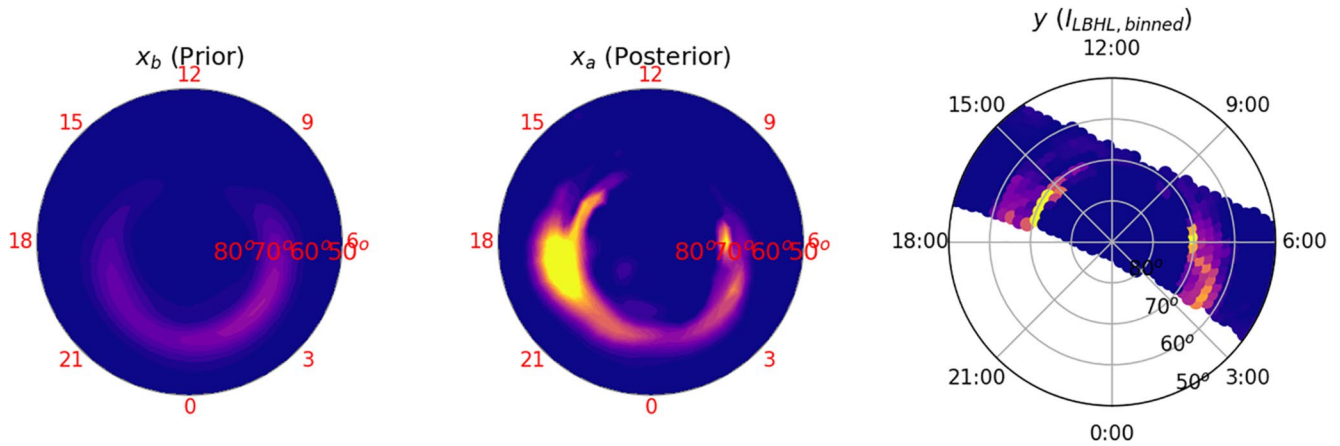
Figure 7. Assimilative mapping of LBHL emissions for the Northern Hemispheric pass by DMSP F16 February 22nd 2:37 UTC shown in the same format as Figure 6. The dynamic range for all subplots is 0–2 kilorayleighs with darker colors indicating smaller radiance in the linear color contour scale defined as the colorbar for Figure 2.
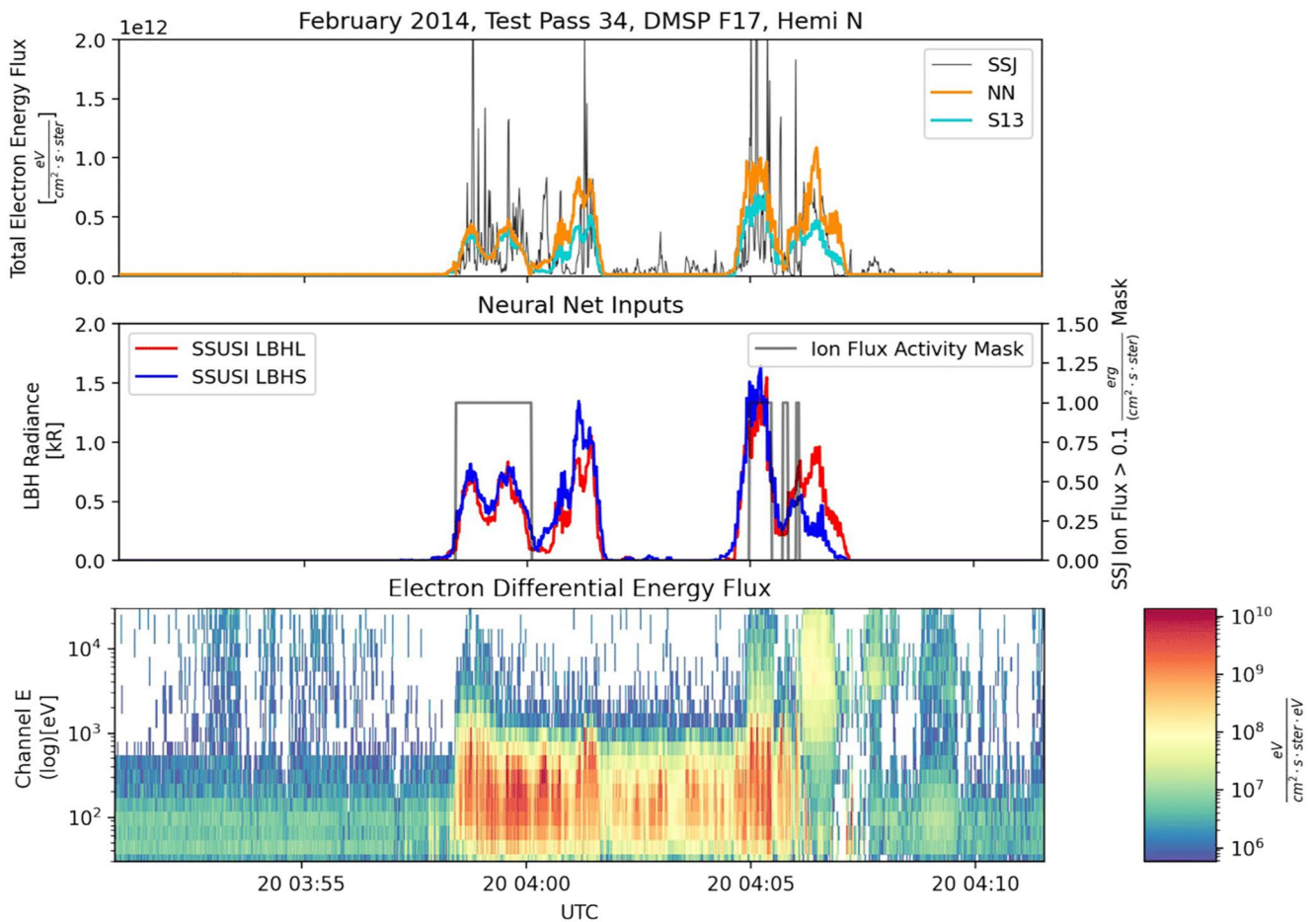

Figure 8. Neural network model prediction of auroral electron energy flux for the same Northern Hemisphere satellite pass shown in Figure 1 by DMSP F17 at 4:02 UTC on February 20th. Top: Neural network (NN) and S13 predictions along with observed electron total energy flux by special sensor J (SSJ). Middle: Input data: scaled $I_{LBHL, smoothed}$, $I_{LBHS, smoothed}$, and ion flux activity mask M_I. Bottom: Electron energy spectrogram recorded by SSJ shown in log-scale.
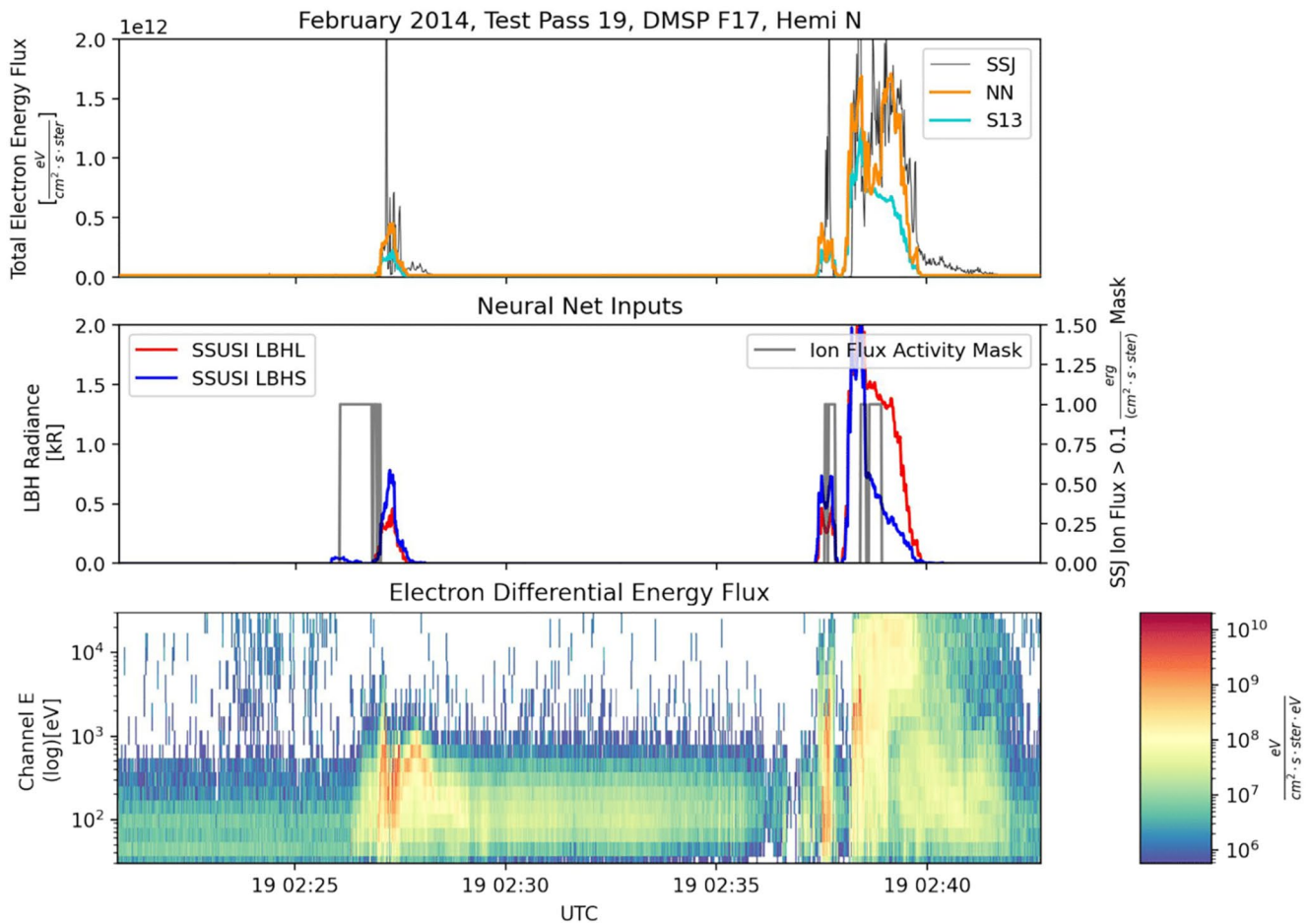
Figure 9. Neural network model prediction of auroral electron energy flux for the Northern Hemisphere satellite pass by DMSP F17 at 2:32 UTC on February 19th, displayed in the same format as Figure 8.

pronounced for higher activity passes. Table 4 shows the RMSE prediction error for AE levels higher or lower that 450 nT. Under geomagnetically active conditions, the RMSE value for the neural network prediction is worse in comparison to quiet times, even though the higher signal-to-noise data available during active times yields a better performance measured in terms of the correlations. These RMSE values is also likely influenced by significant outlier flux values detected by the SSJ instrument. When compared to the RMSE of the S13 prediction error, we note a better overall performance of the neural network model for active passes. For less active passes, the S13 model has a significantly lower RMSE than the neural network model prediction. This difference may be attributed to the result of lower signal-to-noise of input signals during geomagnetic quiet times with the use of additional input features in training of the neural network model.

5. Use Case: Assimilative Mapping of Auroral Energy Flux

This section presents a use case for the assimilative mapping procedure of auroral energy flux developed using a combination of three data-driven approaches described in Section 2.4 for DMSP F17 Northern Hemisphere high-latitude overpass at 4.02 UTC on February 20th. As shown in the workflow of the procedure depicted in Figure 3, the procedure first yields assimilative maps of LBHL and LBHS emission which are then transformed into assimilative maps of auroral electron energy flux using the neural network predictive model. This neural network model requires a map of the ion flux activity mask in addition to assimilative maps of LBHL and LBHS emission, but the ion energy flux information from the SSJ instrument is not available outside of the DMSP spacecraft track. The ion flux activity mask is thus built using ion flux from the Ovation Prime model (Newell et al., 2009). The left plot of Figure 11 shows the Ovation Prime ion energy flux map for February 20th at 4:02
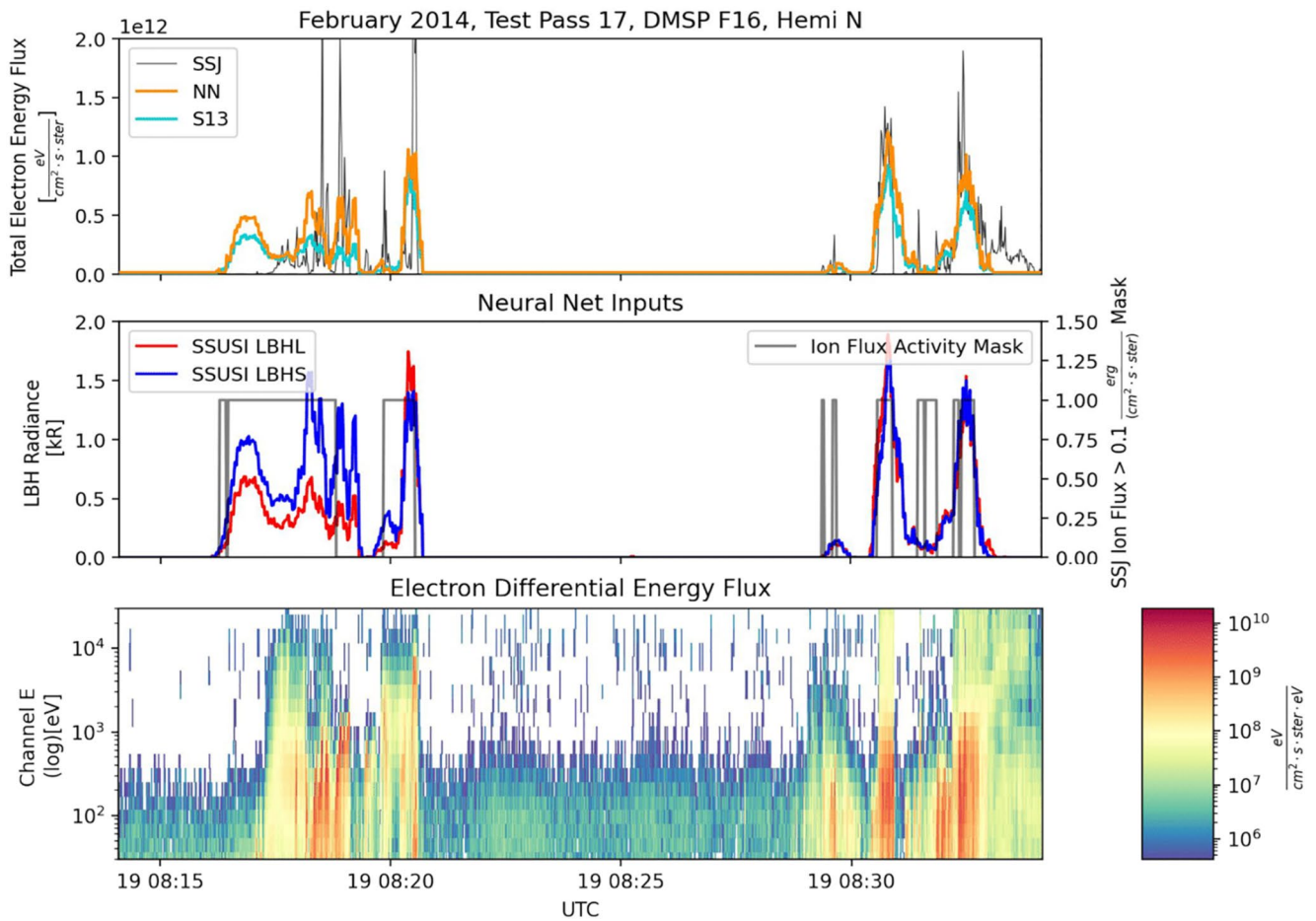
Figure 10. Neural network model prediction of auroral electron energy flux for the Northern Hemisphere satellite pass by DMSP F16 at 8:24 UTC on February 19th, displayed in the same format as Figure 8.

UTC, while the right plot shows a map of the ion flux activity mask with values of 1 where the ion total energy flux is more than $0.1 \frac{ergs}{s \cdot cm^2}$ and 0 elsewhere. Note that the small unphysical feature present around noon results from a known artifact of the 2010 Ovation Prime model (Newell et al., 2014). Figure 12 presents the assimilative mapping result of auroral energy flux using LBHL and LBHS emission data from the DMSP F17 pass over the Northern Hemisphere at 4:02 UTC on February 20th. This is the same pass shown in Figure 1. This use case shows how the proposed end-to-end data-driven modeling approach can transform partial images of LBH emission from the SSUSI instrument into global assimilative maps of auroral electron energy flux, demonstrating a new exciting data assimilative mapping capability expected to expand the usage of currently available space-based FUV imagers to address pressing MIT science questions discussed in the introduction section.

6. Discussion and Future Work

In this section, we discuss the future work required to overcome some limitations identified in this study. Although the data preprocessing steps to remove solar influence from the SSUSI SDR data product described in Section 2.3.1 has worked effectively for most DMSP satellite hemispheric passes, some passes still exhibit significant noise. This noise coupled with the relatively high dynamic range of the LBH emission creates a unique challenge to data-driven modeling using LBH emission data, impacting not only the quality of the neural network modeling, EOF analysis and OI presented in this study but also any attempts to extract physical parameters from LBH emission

Table 3
Pearson Correlation Between Prediction and Test Data

Median AE index	NN	S13
AE > 450	0.74	0.59
AE < 450	0.62	0.40
All Conditions	0.71	0.59

Table 4
Auroral Energy Flux RMSE Prediction Error $\left[\frac{eV}{cm^2 \cdot sr \cdot s}\right]$

AE index	NN	S13
AE > 450	5.6833e11	7.612e11
AE < 450	2.2205e11	6.28e10
All Conditions	3.1828e11	3.84e11

data. In the future, it may be helpful to set up a quality flag to automatically exclude these passes from training. Issues can also be overcome by increasing the amount of data to be fed into a neural network and EOF non-linear regression analysis, which effectively increases the signal-to-noise ratio. The uncertainty associated with the solar influence removal can be incorporated into the OI in the form of an observational error covariance with spatially correlated errors. In order to cover a wide range of geophysical conditions and improve statistical confidence of analysis results in the future, it is imperative to learn global modes (e.g., EOF) of LBH emission variability and a neural network predictive model of auroral energy from a much larger data set of SSUSI and SSJ observations than 1 week used for demonstration of the data-driven modeling approach developed in this study.

In this paper, LBH emission data from both hemispheres are used to create a universal EOF set to overcome this limitation. Even with the use of data from both hemispheres, inhomogeneous sampling of LBH emission by DMSP satellites will likely present a challenge to EOF analysis. Figure 13 shows the total number of spatially binned LBHL observations available at each bin location across the week of data used. The lack of data coverage in both the day and nightside mid-latitude regions is evident. Although the EOF analysis has attempted to mitigate the data gap issues through the usage of the Tikhonov regularization, it results in some unphysical features present in EOF patterns as shown in Figure 5. To further reduce the effect of the data gap in the future, additional regularization techniques can be applied as well as the incorporation of weighted observation errors following the methods of Cousins et al. (2013).

In addition to improvements of neural network predictive modeling of auroral electron energy flux from LBH emission with the use of more SSUSI-SSJ conjunction data, one future avenue is to automate the optimization of hyper-parameters of the neural network using techniques such as cross validation and genetic algorithms instead of analyzing the validation results and tuning the model structure with hopes of finding the optimal structure manually. As mentioned briefly in Section 3.3, considerable difficulties arise in distinguishing the contributions from precipitating ions from precipitating electrons to LBH radiance. Although we present some success with our neural network model performance, this model is still limited in its capacity to predict electron total energy flux as a result of several geophysical factors. Previous estimates have shown that precipitating protons may be approximately 5 times more efficient per unit of energy flux than precipitating electrons in their production of LBH radiance (Knight et al., 2012). Different physical processes, such as excitation via direct electron impact and cascading induced excitation, are known to contribute to LBH emissions to an uncertain extent
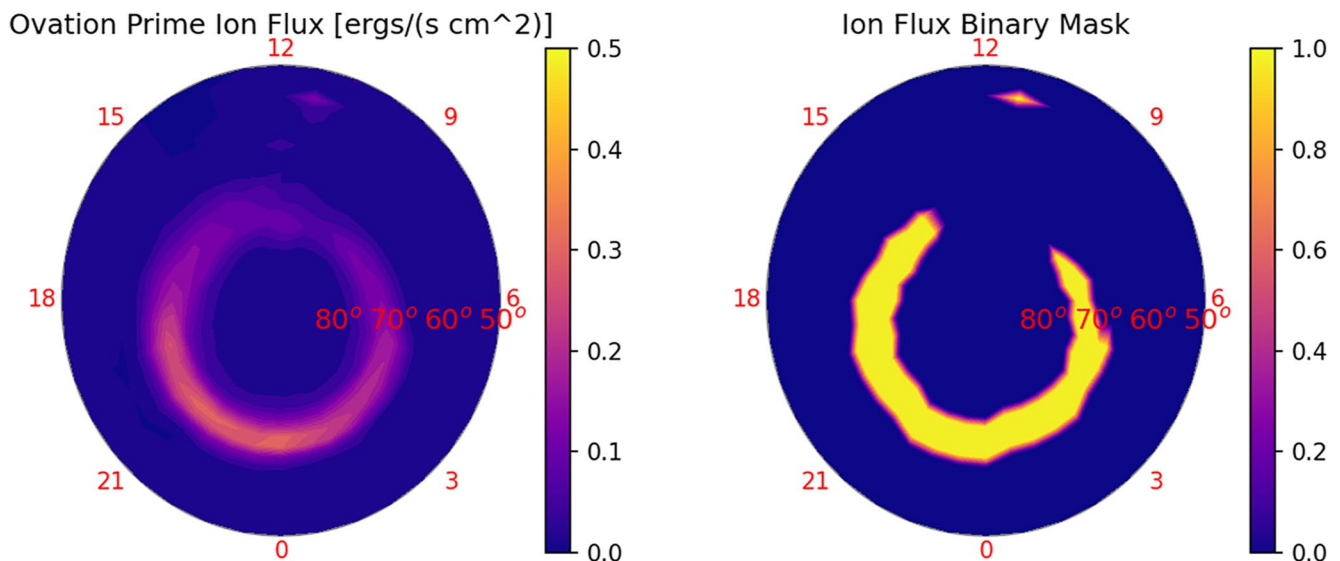

Figure 11. Left: Map of ion flux from the Ovation Prime model on February 20th, 4:02 UTC. Right: Map of ion flux activity mask (M_I) derived from the Ovation Prime ion flux.
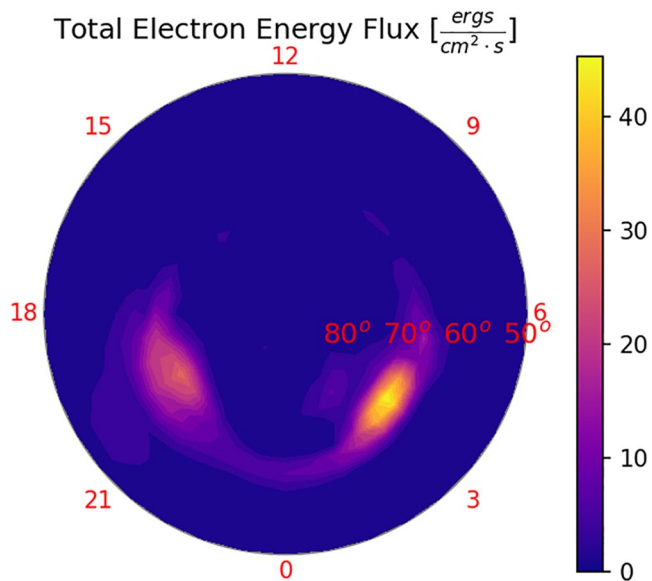
Figure 12. Assimilative mapping of auroral electron energy flux using SSUSI LBH emission data from the DMSP F17 pass over the Northern Hemisphere at 4:02 UTC on February 20th. This is the same pass shown in Figure 1.

(Ajello et al., 2020). Such uncertainty, in tandem with the lack of in-situ ion precipitation measurements outside the spacecraft track, poses significant challenges. A separate model to predict auroral ion energy flux using the SSUSI LBH emission data alongside SSUSI H lyman-alpha band emission data, following the work of (Knight et al., 2012), could help to reduce the uncertainty introduced by the use of ion flux activity mask built using the Ovation Prime model in the assimilative mapping procedure. Another important avenue for future work is to address the validation of off-nadir SSUSI data. Off-nadir training data with the SSJ instrument would require multiple DMSP spacecraft simultaneously sampling the same magnetic latitude and local time region. Since these are rare events, to build up sufficient training data for off-nadir conjunctions, it is necessary to use a much larger time frame of data. Lastly, the neural network model is predicting electron flux from two FUV integrated radiance bands in this study, however, the SSUSI instrument is also capable of recording hyperspectral images, where, for each observation pixel, one can observe differential radiances across the full FUV spectrum. It may be interesting to explore if a predictive skill of the neural network model can be improved from the usage of the full LBH FUV spectrum. In addition to validation of the neural network model, cross validation of the final assimilation results of auroral energy flux against independent electron precipitation data (e.g., FAST, POES, etc) is a critical step in the future development of a production version of the model. With a fully developed model, comparisons against other existing auroral energy flux models (e.g., OVATION Prime) can be made using metrics such as hemispherically integrated electron energy flux.
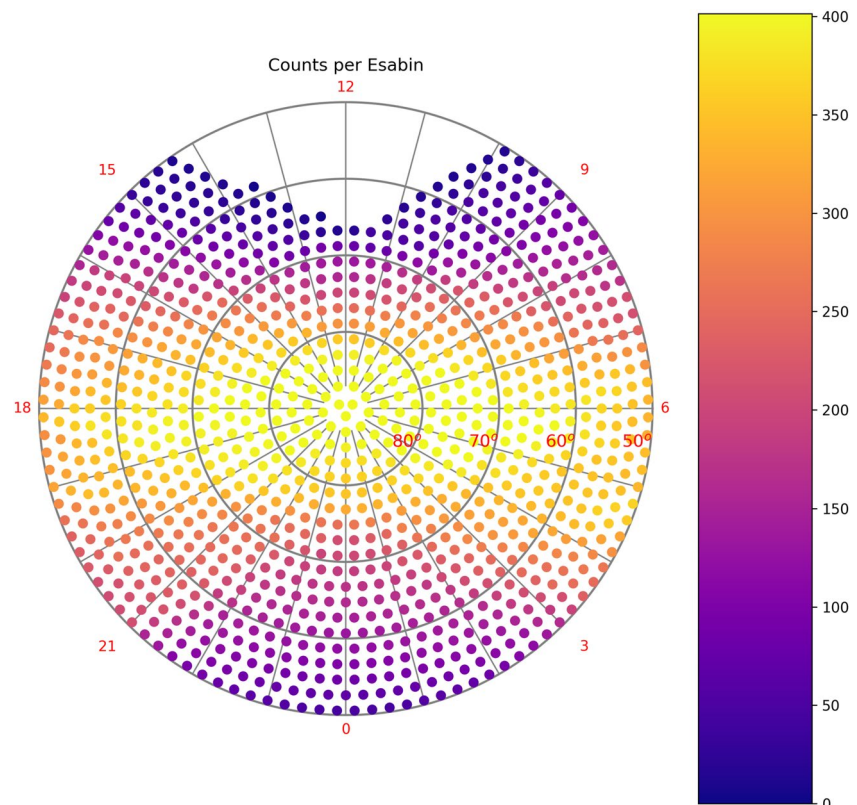

Figure 13. Total spatial coverage of LBHL observations from both Northern and Southern Hemisphere passes in the Apex geomagnetic coordinates.

7. Conclusions

In this study, we have developed a new data-driven modeling approach that allows direct ingestion of satellite LBH emission imager data into global instantaneous assimilative mappings of electron total energy flux unlike in past assimilative mapping approaches wherein retrieved emission products are used (e.g., Lu, 2017, references therein). This is achieved through the combination of three machine learning techniques described in Section 2.3: defining modes of variability through the usage of EOFs, spatial prediction of LBH emission using OI, and relating LBH emission to precipitating electron energy flux with neural network modeling. The dominant modes of auroral emission variability estimated using 1 week of the SSUSI data in this work are found to be generally consistent with the dominant modes of auroral Pedersen and Hall conductance which were determined from a large volume of the SSJ data by R. McGranaghan et al. (2015). Within the limited scope of comparison over 17–23 February 2014, a new nonlinear empirical model to predict auroral electron energy flux from LBH emission data trained using the neural network outperforms the linear empirical model predicting electron total energy flux from LBHL emission outlined in Sotirelis et al. (2013), yielding better out-of-sample prediction skills measured in terms of correlation and RMSE, especially under higher geomagnetic activity conditions. This highlights neural network's ability to account for a non-linear relationship between LBH emission and auroral energy flux and underscores the efficacy of the use of ion flux information as an additional input feature in training. With more training data and validation of the neural network model and EOFs, the end-to-end data driven modeling approach developed in this study has the potential to achieve a greater spatial predictive performance than demonstrated with limited amounts of data in this study. Finally, with details of data provenance and data analysis steps, this paper serves as a blueprint for future comprehensive development efforts for a data-driven approach to auroral energy flux that can take advantage of the wider spatial coverage provided by over 12 years of SSUSI FUV emission data. A fully developed and validated data assimilative mapping capability can be incorporated into the AMGeO open source software (AMGeO Collaboration, 2019; Matsuo, 2020) to address science questions regarding global auroral dynamics including but not limited to substorm surges, hemispheric asymmetry, and dawn-dusk asymmetry of the aurora.

Data Availability Statement

The publicly available solar wind and geomagnetic activity indices data are obtained from the GSFC Space Physics Data Facility OMNIWeb FTP interface at https://omniweb.gsfc.nasa.gov. All the results presented in this paper are produced from publicly accessible data sets using the following open source software tools available from respective repositories or as part of Python open source packages. The code used for the optimal interpolation of LBH emissions is part of the AMGeO open source software (https://doi.org/10.5281/zenodo.3564915) available upon registration at https://amgeo.colorado.edu/. The code used to preprocess the SSUSI and SSJ data, create SSUSI-SSJ conjunction data sets, and train the neural network model is available as open source software (https://doi.org/10.5281/zenodo.4587943) at https://zenodo.org/record/4587943. We acknowledge the use of following Python open source packages: Numpy, Scikit-Learn, SciPy, and Keras.

References

Ajello, J. M., Evans, J. S., Veibell, V., Malone, C. P., Holsclaw, G. M., Hoskins, A. C., et al., (2020). The UV spectrum of the lyman-Birge-Hopfield band system of N2 induced by cascading from electron impact. *Journal of Geophysical Research: Space Physics*, *125*(3), e2019JA027546. Retrieved on 2021-02-24, https://doi.org/10.1029/2019JA027546

Akasofu, S. I. (1964). The development of the auroral substorm. *Planetary and Space Science*, *12*(4), 273–282. Retrieved 2021-02-21, https://doi.org/10.1016/0032-0633(64)90151-5

AMGeO Collaboration. (2019). *A Collaborative data science platform for the geospace Community: Assimilative mapping of geospace observations (AMGeO) v1.0.0 (Tech. Rep.)*. Retrieved on 2021-01-12, https://doi.org/10.5281/zenodo.3564914

Asikainen, T., & Mursula, K. (2013). Correcting the NOAA/MEPED energetic electron fluxes for detector efficiency and proton contamination. *Journal of Geophysical Research: Space Physics*, *118*(10), 6500–6510. Retrieved 2021-03-11, https://doi.org/10.1002/jgra.50584

Burch, J. L., Mende, S. B., Mitchell, D. G., Moore, T. E., Pollock, C. J., Reinisch, B. W., et al. (2001). Views of Earth's magnetosphere with the IMAGE satellite. *Science*, *291*(5504), 619–624. Retrieved 2021-03-10, https://doi.org/10.1126/science.291.5504.619

Christensen, A. B., Paxton, L. J., Avery, S., Craven, J., Crowley, G., Humm, D. C., et al. (2003). Initial observations with the global ultraviolet imager (GUVI) in the NASA TIMED satellite mission. *Journal of Geophysical Research: Space Physics*, *108*(A12), 1451. Retrieved on 2021-03-10, https://doi.org/10.1029/2003JA009918

Cousins, E. D. P., Matsuo, T., & Richmond, A. D. (2013). SuperDARN assimilative mapping. *Journal of Geophysical Research: Space Physics*, *118*(12), 7954–7962. Retrieved on 2021-01-11, https://doi.org/10.1002/2013JA019321

Cousins, E. D. P., Matsuo, T., & Richmond, A. D. (2015). Mapping high-latitude ionospheric electrodynamics with SuperDARN and AMPERE. *Journal of Geophysical Research: Space Physics*, *120*(7), 5854–5870. Retrieved on 2021-03-14, https://doi.org/10.1002/2014JA020463

Durgonics, T., Komjathy, A., Verkhoglyadova, O., Shume, E. B., Benzon, H.-H., Mannucci, A. J., et al. (2017). Multiinstrument observations of a geomagnetic storm and its effects on the Arctic ionosphere: A case study of the 19 February 2014 storm. *Radio Science*, *52*(1), 146–165. Retrieved on 2021-01-22, https://doi.org/10.1002/2016RS006106

Fillingim, M. O., Parks, G. K., Frey, H. U., Immel, T. J., & Mende, S. B. (2005). Hemispheric asymmetry of the afternoon electron aurora. *Geophysical Research Letters*, *32*(3), L03113. Retrieved on 2021-02-22, https://doi.org/10.1029/2004GL021635

Gaspari, G., & Cohn, S. E. (1999). Construction of correlation functions in two and three dimensions. *Quarterly Journal of the Royal Meteorological Society*, *125*(554), 723–757. Retrieved on 2021-01-24, https://doi.org/10.1002/qj.49712555417

Germany, G. A., Spann, J. F., Parks, G. K., Brittnacher, M. J., Elsen, R., Chen, L., et al. (1998). Auroral observations from the POLAR ultraviolet imager (UVI). In *Geospace mass and energy Flow* (pp. 149–160). American Geophysical Union (AGU). Retrieved on 2021-03-10, https://doi.org/10.1029/GM104p0149

Ghamry, E., Lethy, A., Arafa-Hamed, T., & Abd Elaal, E. (2016). A comprehensive analysis of the geomagnetic storms occurred during 18 February and 2 March 2014. *NRIAG Journal of Astronomy and Geophysics*, *5*(1), 263–268. Retrieved on 2021-01-19, https://doi.org/10.1016/j.nrjag.2016.03.001

Hardy, D. A., Gussenhoven, M. S., & Brautigam, D. (1989). A statistical model of auroral ion precipitation. *Journal of Geophysical Research: Space Physics*, *94*(A1), 370–392. Retrieved on 2021-03-11, https://doi.org/10.1029/JA094iA01p00370

Hardy, D. A., Holeman, E. G., Burke, W. J., Gentile, L. C., & Bounar, K. H. (2008). Probability distributions of electron precipitation at high magnetic latitudes. *Journal of Geophysical Research: Space Physics*, *113*(A6), A06305. Retrieved on 2021-01-17, https://doi.org/10.1029/2007JA012746

Hopkins University, J. Applied physics Laboratory SSUSI Team. (2013). *SSUSI data products algorithms version 1.12*.

Kingma, D. P., & Ba, J. (2017). *Adam: A method for Stochastic optimization*. arXiv:1412.6980 [cs]. Retrieved on 2021-01-15, Retrieved from http://arxiv.org/abs/1412.6980

Knight, H. K., & Strickland, D. (2013). Comment on "Empirical relationship between electron precipitation and far-ultraviolet auroral emissions from DMSP observations" by Sotirelis et al. *Journal of Geophysical Research: Space Physics*, *118*(10), 6823–6826. Retrieved on 2020-12-24, https://doi.org/10.1002/jgra.50505

Knight, H. K., Strickland, D. J., Correira, J., Hecht, J. H., & Straus, P. R. (2012). An empirical determination of proton auroral far ultraviolet emission efficiencies using a new nonclimatological proton flux extrapolation method. *Journal of Geophysical Research: Space Physics*, *117*(A11), A11316. Retrieved on 2021-01-26, https://doi.org/10.1029/2012JA017672

Liou, K., & Mitchell, E. J. (2020a). Hemispheric asymmetry of the dayside aurora due to imbalanced solar insolation. *Scientific Reports*, 10(1), 13451. Retrieved on 2021-02-17, from Nature Publishing Group. https://doi.org/10.1038/s41598-020-70018-w

Liou, K., & Mitchell, E. J. (2020b). Hemispheric asymmetry of the dayside aurora due to imbalanced solar insolation. *Scientific Reports*, *10*(1), 13451. Retrieved on 2021-02-19, https://doi.org/10.1038/s41598-020-70018-w

Lu, G. (2017). Large scale high-latitude ionospheric electrodynamic fields and currents. *Space Science Reviews*, *206*(1), 431–450. Retrieved on 2021-02-13, https://doi.org/10.1007/s11214-016-0269-9

Matsuo, T. (2020). Recent progress on inverse and data assimilation procedure for high-latitude ionospheric electrodynamics. In M. W.Dunlop & H.Lühr (Eds.), *Ionospheric multi-spacecraft analysis tools: Approaches for deriving ionospheric parameters* (pp. 219–232). Cham: Springer International Publishing. Retrieved from https://doi.org/10.1007/978-3-030-26732-2_10

Matsuo, T., Knipp, D. J., Richmond, A. D., Kilcommons, L., & Anderson, B. J. (2015). Inverse procedure for high-latitude ionospheric electrodynamics: Analysis of satellite-borne magnetometer data. *Journal of Geophysical Research: Space Physics*, *120*(6), 5241–5251. Retrieved on 2021-03-14, https://doi.org/10.1002/2014JA020565

Matsuo, T., Richmond, A. D., & Lu, G. (2005). Optimal interpolation analysis of high-latitude ionospheric electrodynamics using empirical orthogonal functions: Estimation of dominant modes of variability and temporal scales of large-scale electric fields. *Journal of Geophysical Research: Space Physics*, *110*(A6), A06301. Retrieved on 2021-03-14, https://doi.org/10.1029/2004JA010531

Matsuo, T., Richmond, A. D., & Nychka, D. W. (2002). Modes of high-latitude electric field variability derived from DE-2 measurements: Empirical Orthogonal Function (EOF) analysis. *Geophysical Research Letters*, *29*(7), 11-1–11-4. Retrieved on 2020-12-24, https://doi.org/10.1029/2001GL014077

McCulloch, W. S., & Pitts, W. (1943). A logical calculus of the ideas immanent in nervous activity. *Bulletin of Mathematical Biophysics*, *5*(4), 115–133. https://doi.org/10.1007/bf02478259

McGranaghan, R., Knipp, D. J., Matsuo, T., & Cousins, E. (2016). Optimal interpolation analysis of high-latitude ionospheric Hall and Pedersen conductivities: Application to assimilative ionospheric electrodynamics reconstruction. *Journal of Geophysical Research: Space Physics*, *121*(5), 4898–4923. Retrieved on 2020-12-24, https://doi.org/10.1002/2016JA022486

McGranaghan, R., Knipp, D. J., Matsuo, T., Godinez, H., Redmon, R. J., Solomon, S. C., & Morley, S. K. (2015). Modes of high-latitude auroral conductance variability derived from DMSP energetic electron precipitation observations: Empirical orthogonal function analysis. *Journal of Geophysical Research: Space Physics*, *120*(12), 11013–11031. Retrieved on 2021-02-04, https://doi.org/10.1002/2015JA021828

McGranaghan, R. M., Ziegler, J., Bloch, T., Hatch, S., Camporeale, E., Lynch, K., et al. (2021). Toward a next generation particle precipitation model: Mesoscale prediction through machine learning (a case study and Framework for Progress). *Space Weather*, *19*(6), e2020SW002684. Retrieved on 2021-12-01, https://doi.org/10.1029/2020SW002684

Newell, P. T., Liou, K., Zhang, Y., Sotirelis, T., Paxton, L. J., & Mitchell, E. J. (2014). OVATION Prime-2013: Extension of auroral precipitation model to higher disturbance levels. *Space Weather*, *12*(6), 368–379. Retrieved on 2021-01-26, https://doi.org/10.1002/2014SW001056

Newell, P. T., Sotirelis, T., & Wing, S. (2009). Diffuse, monoenergetic, and broadband aurora: The global precipitation budget. *Journal of Geophysical Research: Space Physics*, *114*(A9), A09207. Retrieved on 2021-01-18, https://doi.org/10.1029/2009JA014326

Omohundro, S. M. (1989). *Five balltree construction algorithms* (Tech Report) (pp. 1–22). International Computer Science Institute.

Østgaard, N., Tsyganenko, N. A., Mende, S. B., Frey, H. U., Immel, T. J., Fillingim, M., & Sigwarth, J. B. (2005). Observations and model predictions of substorm auroral asymmetries in the conjugate hemispheres. *Geophysical Research Letters*, *32*(5), L05111. Retrieved on 2021-02-22, https://doi.org/10.1029/2004GL022166

Paxton, L. J., Morrison, D., Zhang, Y., Kil, H., Wolven, B., Ogorzalek, B. S., et al. (2002). Validation of remote sensing products produced by the special sensor ultraviolet Scanning imager (SSUSI): A far UV-imaging spectrograph on DMSP F-16. In *Optical Spectroscopic techniques, remote sensing, and Instrumentation for atmospheric and space Research IV* (Vol. 4485, pp. 338–348). International Society for Optics and Photonics. Retrieved on 2021-03-10, https://doi.org/10.1117/12.454268

Redmon, R. J., Denig, W. F., Kilcommons, L. M., & Knipp, D. J. (2017). New DMSP database of precipitating auroral electrons and ions. *Journal of Geophysical Research: Space Physics*, *122*(8), 9056–9067. Retrieved on 2020-12-24, https://doi.org/10.1002/2016JA023339

Richmond, A. D. (1995). Ionospheric electrodynamics using magnetic Apex coordinates. *Journal of Geomagnetism and Geoelectricity*, *47*(2), 191–212. Retrieved on 2021-03-23, https://doi.org/10.5636/jgg.47.191

Richmond, A. D., & Kamide, Y. (1988). Mapping electrodynamic features of the high-latitude ionosphere from localized observations: Technique. *Journal of Geophysical Research: Space Physics*, *93*(A6), 5741–5759. Retrieved on 2021-01-15, https://doi.org/10.1029/JA093iA06p05741

Rifkin, R. M., & Lippert, R. A. (2007). *Notes on regularized least squares* (Tech Report, MIT-CSAIL-TR-2007-025). Massachusetts Institute of Technology Computer Science and Artificial Intelligence Laboratory.

Robinson, R. M., Vondrak, R. R., Miller, K., Dabbs, T., & Hardy, D. (1987). On calculating ionospheric conductances from the flux and energy of precipitating electrons. *Journal of Geophysical Research: Space Physics*, *92*(A3), 2565–2569. Retrieved on 2021-03-20, https://doi.org/10.1029/JA092iA03p02565

Robinson, R. M., Zhang, Y., Anderson, B. J., Zanetti, L. J., Korth, H., & Fitzmaurice, A. (2018). Statistical relations between field-aligned currents and precipitating electron energy flux. *Geophysical Research Letters*, *45*(17), 8738–8745. Retrieved from https://doi.org/10.1029/2018GL078718

Shi, Y., Knipp, D. J., Matsuo, T., Kilcommons, L., & Anderson, B. (2020). Modes of (FACs) variability and their hemispheric asymmetry revealed by inverse and assimilative analysis of Iridium magnetometer data. *Journal of Geophysical Research: Space Physics*, *125*(2), e2019JA027265. Retrieved on 2021-01-23, https://doi.org/10.1029/2019JA027265

Sicard-Piet, A., Bourdarie, S., Boscher, D., Friedel, R. H. W., Thomsen, M., Goka, T., et al. (2008). A new international geostationary electron model: IGE-2006, from 1 keV to 5.2 MeV. *Space Weather*, *6*(7), S07003. Retrieved on 2021-03-11, https://doi.org/10.1029/2007SW000368

Solomon, S. C. (2017). Global modeling of thermospheric airglow in the far ultraviolet. *Journal of Geophysical Research: Space Physics*, *122*(7), 7834–7848. Retrieved on 2021-01-14, https://doi.org/10.1002/2017JA024314

Sotirelis, T., Korth, H., Hsieh, S.-Y., Zhang, Y., Morrison, D., & Paxton, L. (2013). Empirical relationship between electron precipitation and far-ultraviolet auroral emissions from DMSP observations. *Journal of Geophysical Research: Space Physics*, *118*(3), 1203–1209. Retrieved on 2020-12-24, https://doi.org/10.1002/jgra.50157

Spiro, R. W., Reiff, P. H., & Maher, L. J. (1982). Precipitating electron energy flux and auroral zone conductances-An empirical model. *Journal of Geophysical Research: Space Physics*, *87*(A10), 8215–8227. Retrieved on 2021-03-11, https://doi.org/10.1029/JA087iA10p08215

Strickland, D. J., Bishop, J., Evans, J. S., Majeed, T., Shen, P. M., Cox, R. J., et al. (1999). Atmospheric ultraviolet radiance integrated code (AURIC): Theory, software architecture, inputs, and selected results. *Journal of Quantitative Spectroscopy and Radiative Transfer*, *62*(6), 689–742. Retrieved on 2020-12-29, https://doi.org/10.1016/S0022-4073(98)00098-3

Strickland, D. J., Daniell, R. E., Jasperse, J. R., & Basu, B. (1993). Transport-theoretic model for the electron-proton-hydrogen atom aurora: 2. Model results. *Journal of Geophysical Research: Space Physics*, *98*(A12), 21533–21548. Retrieved on 2021-02-12, https://doi.org/10.1029/93JA01645

Xu, B., Wang, N., Chen, T., & Li, M. (2015). *Empirical evaluation of rectified activations in Convolutional network*.

Zhou, X.-Y., Fukui, K., Carlson, H. C., Moen, J. I., & Strangeway, R. J. (2009). Shock aurora: Ground-based imager observations: SHOCK aurora-ground-based observations. *Journal of Geophysical Research: Space Physics*, *114*(A12), A12216. Retrieved on 2021-02-17, https://doi.org/10.1029/2009JA014186

Zhou, X.-Y., Strangeway, R. J., Anderson, P. C., Sibeck, D. G., Tsurutani, B. T., Haerendel, G., et al. (2003). Shock aurora: FAST and DMSP observations. *Journal of Geophysical Research: Space Physics*, *108*(A4), 8019. Retrieved on 2021-02-22, https://doi.org/10.1029/2002JA009701